Chapter 7
Hall Thrusters

7.1 Introduction

Hall thrusters are relatively simple devices consisting of a cylindrical channel with an interior anode, a magnetic circuit that generates a primarily radial magnetic field across the channel, and a cathode external to the channel. However, Hall thrusters rely on much more complicated physics than ion thrusters to produce thrust. The details of the channel structure and magnetic field shape determine the performance, efficiency, and life [1–5]. The efficiency and specific impulse of flight-model Hall thrusters are typically lower than that achievable in ion thrusters [6,7], but the thrust-to-power ratio is higher and the device requires fewer power supplies to operate. The life of Hall thrusters in terms of hours of operation is usually shorter than ion thrusters (on the order of 10,000 hours), but the throughput is usually higher than in ion thrusters, and the total impulse capability can be comparable. Hall thrusters were originally envisioned in the U.S. and Russia about 50 years ago, with the first working devices reported in America in the early 1960s. Ultimately, Hall thruster technology was developed to flight status in Russia and has only recently been developed and flown outside of that country. Information about flight Hall thrusters is given in Chapter 9.

There are two generic types of Hall thrusters described in the literature. Hall thrusters, Hall-effect thrusters (HETs), stationary plasma thrusters (SPTs), and magnetic-layer thrusters are all names for essentially the same device that is characterized by the use of a dielectric insulating wall in the plasma channel, as illustrated in Fig. 7-1. The wall is typically manufactured from dielectric materials such as boron nitride (BN) or borosil ($BN\text{-}SiO_2$) in flight thrusters, and also sometimes alumina (AL_2O_3) in laboratory thrusters. These dielectric materials have a low sputtering yield and relatively low secondary

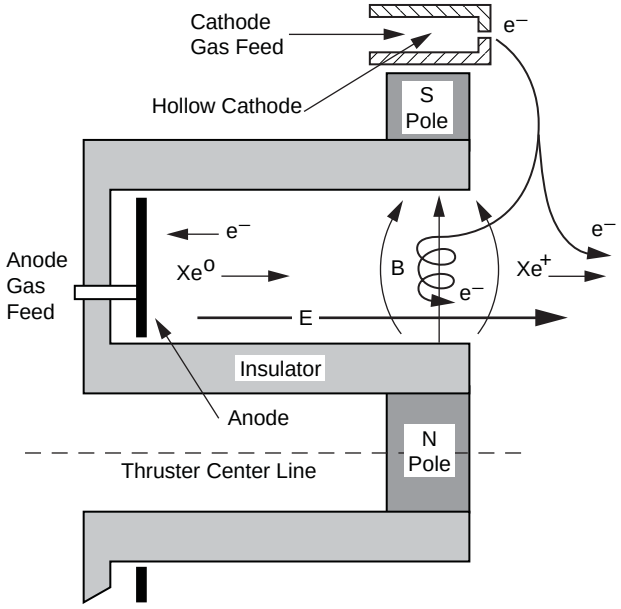

Fig. 7-1. Hall thruster cross-section schematic showing the crossed electric and magnetic fields, and the ion and electron paths.

electron emission coefficients under xenon ion bombardment. In this thruster geometry, the electrically biased metallic anode is positioned at the base of the channel where the majority of the propellant gas is injected into the thruster. The remainder of the propellant gas used by the thruster is injected through the exterior hollow cathode. In the second version of this type of thruster, called a thruster with anode layer (TAL), the dielectric channel wall is replaced by a metallic conducting wall, as illustrated in Fig. 7-2. This geometry considerably shortens the electric field region in the channel where the ion acceleration occurs—hence the name “thruster with anode layer” from the Russian literature [1], associated with the narrow electric field region near the anode. However, this configuration does not change the basic ion generation or acceleration method. The channel wall, which is usually also part of the magnetic circuit, is biased negatively (usually cathode potential) to repel electrons in the ionization region and reduce electron-power losses. The defining differences between these two types of Hall thrusters have been described in the literature [3].

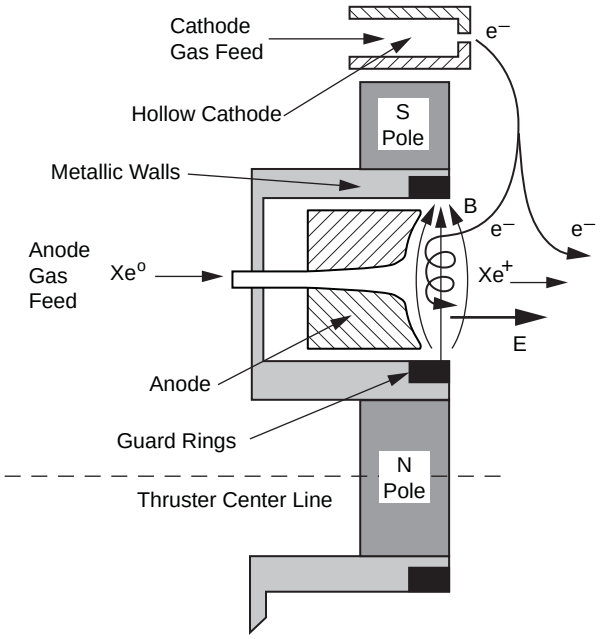

Fig. 7-2. TAL thruster cross-section schematic showing the crossed electric and magnetic fields, and the ion and electron paths.

In the Hall thruster with dielectric walls illustrated in Fig. 7-1, an axial electric field is established between the anode at the base of an annular channel and the hollow-cathode plasma produced outside of the thruster channel. A transverse (radial) magnetic field prevents electrons from this cathode plasma from streaming directly to the anode. Instead, the electrons spiral along the magnetic field lines (as illustrated) and in the $\mathbf{E} \times \mathbf{B}$ azimuthal direction (into the page) around the channel, and they diffuse by collisional processes and electrostatic fluctuations to the anode and channel walls. The plasma discharge generated by the electrons in the crossed electric and magnetic fields efficiently ionizes the propellant injected into the channel from the anode region. Ions from this plasma bombard and, near the channel exit, sputter erode the dielectric walls, which ultimately determines the life of the thruster. Electrons from this plasma also bombard the dielectric wall, depositing a significant amount of power in this region. The reduced axial electron mobility produced by the transverse magnetic field permits the applied discharge voltage to be distributed along the channel axis in the quasi-neutral plasma, resulting in an axial electric field in the channel that accelerates the ions to form the thrust beam. Therefore, Hall thrusters are described as electrostatic devices [1] because the ions are accelerated by the applied electric field, even though a magnetic field is critical to the process. However, since the acceleration occurs in the plasma region near

the channel exit, space charge is not an issue and the ion current density and the thrust density can be considerably higher than that achievable in gridded ion thrusters. The external hollow cathode plasma is not only the source of the electrons for the discharge, but it also provides the electrons to neutralize the ion beam. The single hollow cathode in Hall thrusters serves the same function as the two cathodes in direct current (DC)-electron discharge ion thrusters that produce the plasma and neutralize the beam.

The TAL thruster with metallic walls, illustrated in Fig. 7-2, has the same functional features of the dielectric-wall Hall thruster—namely, an axial electric field is established between the anode in the annular channel and the plasma potential outside of the thruster channel. This field accelerates ions from the ionization region near the anode out of the channel. The transverse (radial) magnetic field again prevents electrons from streaming directly to the anode, and the electron motion is the same as in the dielectric-wall Hall thruster. However, the channel walls at the exit plane have metallic guard rings biased at cathode potential to reduce the electron loss along the field lines. These rings represent the major erosion source in the thruster because of ion bombardment from the plasma, and guard ring material and design often determine the thruster life. The anode typically extends close to the thruster exit and is often funnel-shaped and curved to constrain the neutral gas and plasma to the center of the channel (away from the guard rings) and to not intercept the magnetic field lines, which would cause large electron losses. However, the anode is in close proximity to the high electron-temperature region of the plasma, and electrons collected by the anode can deposit a significant amount of power. The channel width in TAL thrusters is typically twice the channel depth (including the anode shaping). The external hollow cathode plasma provides the electrons for the discharge and for neutralization of the ion beam, the same as for dielectric-wall Hall thrusters.

The azimuthal drift of the electrons around the channel in the crossed electric and magnetic fields in the cylindrical thruster geometry is reminiscent of the *Hall current* in magnetron type devices, which has caused many authors to call this generically a “closed-drift” thruster [1–3]. However, King [8] correctly points out that the orientation of the fields in magnetrons (axial magnetic and radial electric) provides a restoring force to the centrifugal force felt by the electrons as they rotate about the axis, which produces the closed-drift electron motion in magnetrons. There is no corresponding restoring force associated with the different orientation of the crossed fields (radial magnetic and axial electric required to produce axial thrust) in Hall thrusters. The closed-drift behavior of the electron motion in Hall thrusters occurs only because of wall sheath electric fields and the force associated with the magnetic gradient in the radial direction in the channel. In this case, the electrons in the channel

encounter an increasing magnetic field strength as they move toward the wall, which acts as a magnetic mirror to counteract the radial centrifugal force.

The radial magnetic field gradient in the channel also forms an "ion lens," which tends to deflect the ions away from the channel walls and focus the ions out of the channel into the beam. Figure 7-3 shows an example of the magnetic field lines in the NASA-173Mv Hall thruster [9] developed at the National Aeronautics and Space Administration Glenn Research Center (NASA-GRC). The curvature of the field lines in the channel approaching the exit is found to significantly improve the efficiency, especially for higher voltage, high specific impulse (Isp), Hall thrusters [9,10]. The strength of the radial magnetic field in the center along the channel [11] is shown in Fig. 7-4. The radial field peaks near the channel exit and is designed to be essentially zero at or near the anode surface.

7.2 Thruster Operating Principles and Scaling

The operating principles of both types of Hall thrusters and some scaling rules for the geometries can be obtained from a simplified picture of the thruster discharge. Consider a generic Hall thruster channel, shown schematically in cross section in Fig. 7-5. The propellant gas is injected from the left through the anode region and is incident on the plasma generated in the channel. An axial scale length, L, is defined, over which the crossed-field discharge is magnetized, and produces a significant plasma density of width w, which is essentially the channel width. Ions exiting this plasma over the cylindrically

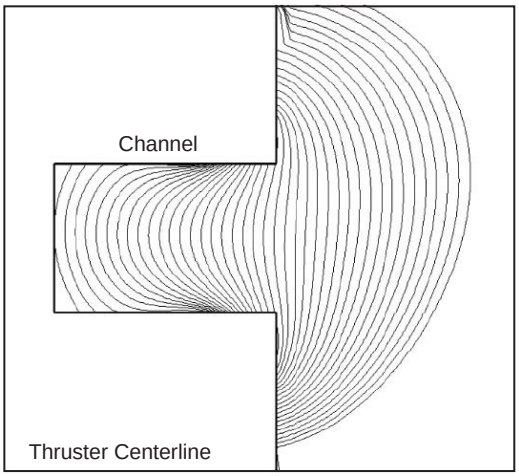

Fig. 7-3. Magnetic field lines in the channel region of the NASA-173Mv Hall thruster (from [9]).

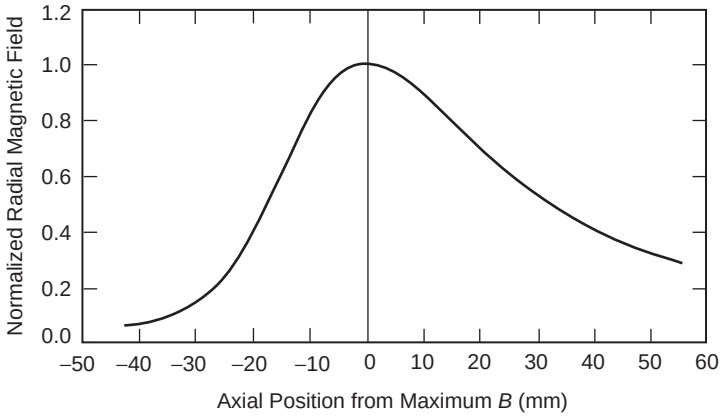

Fig. 7-4. Axial variation centerline radial magnetic field normalized to the peak radial field in the NASA-173Mv Hall thruster (from [11]).

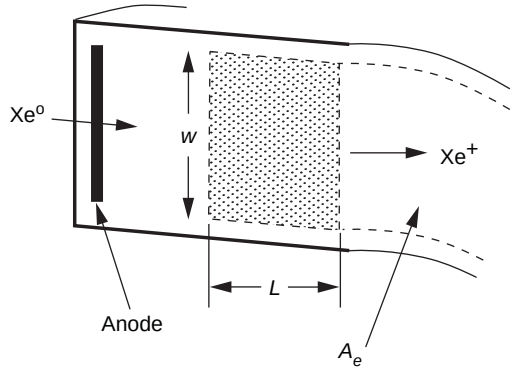

Fig. 7-5. Schematic cross section of the plasma in the Hall thruster channel.

symmetric area A_e form the beam. The applied magnetic field is primarily vertical in the plasma region in this depiction.

7.2.1 Crossed-Field Structure and the Hall Current

The electrons entering the Hall thruster channel from the exterior cathode spiral around the radial magnetic field lines with a Larmor radius derived in Chapter 3 and defined by Eq. (3.3-13). The electron Larmor radius must be less than the characteristic scale length L so that the electrons are magnetized and their mobility to the anode is reduced. If the electron velocity is characterized by their thermal velocity, then the electron Larmor radius is

$$r_e = \frac{v_{th}}{\omega_c} = \frac{m}{eB}\sqrt{\frac{8kT_e}{\pi m}} = \frac{1}{B}\sqrt{\frac{8}{\pi}\frac{m}{e}T_{\mathrm{eV}}} << L\,, \tag{7.2-1}$$

where T_{eV} is the electron temperature in eV and L is the magnetized plasma depth in the channel. For example, the electron Larmor radius at a temperature of 25 eV and a typical radial magnetic field strength of 150 G is 0.13 cm, which is much smaller than typical channel width and plasma length in Hall thrusters. The electrons must also be considered *magnetized*, meaning that they make many orbits around a field line before a collision with a neutral or ion occurs that results in cross-field diffusion. This is normally described by stating that the square of electron Hall parameter must be large compared to unity:

$$\Omega_e^2 = \frac{\omega_c^2}{\nu^2} >> 1, \tag{7.2-2}$$

where ν is the total collision frequency. The effect of this criterion is clear in the expression for the transverse electron mobility in Eq. (3.6-66), where a large value for the Hall parameter significantly reduces the cross-field electron mobility.

In a similar manner, the ion Larmor radius must be much greater than the characteristic channel length so that the ions can be accelerated out of the channel by the applied electric field:

$$r_i = \frac{v_i}{\omega_c} = \frac{M}{eB}\sqrt{\frac{2eV_b}{M}} = \frac{1}{B}\sqrt{\frac{2M}{e}V_b} >> L\,, \tag{7.2-3}$$

where the ion energy is approximated as the beam energy. The ion Larmor radius, for example, in the 150-G radial field and at 300 eV of energy is about 180 cm, which is much larger than the channel or plasma dimensions. These equations provide a general range for the transverse magnetic field in the thruster channel. Even if the radial magnetic field strength doubles or ion energy is half of the example given, the criteria in Eqs. (7.2-1) and (7.2-3) are still easily satisfied.

As mentioned above, the magnetic and electric field profiles are important in the thruster performance and life. The radial magnetic field typically is a maximum near the thruster exit plane, as shown in Fig. 7-4, and it is designed to fall near zero at the anode in dielectric-wall Hall thrusters [12]. Electrons from the cathode experience joule heating in the region of maximum transverse magnetic field, providing a higher localized electron temperature and ionization rate. The reduced electron mobility and high electron temperature in the strong

magnetic field region causes the axial electric field also to be maximized near the exit plane, as illustrated in Fig. 7-6. Since the neutral gas is injected from the anode region and the mass utilization is very high (nearly every neutral is ionized before reaching the channel exit), it is common to describe an "ionization region" that is located upstream of the electric field peak. Of course, the ions are accelerated directly by the electric field that peaks near the exit plane, which is sometimes called the "acceleration region." The characteristic scaling length L then spans these regions and is a significant fraction of the total channel depth. The ionization and acceleration regions overlap, which leads to dispersion in the ion velocity and some angular divergence in the resultant beam. This is in contrast to ion thrusters, which have a distinct ionization region in the plasma chamber and a finite acceleration region in the grids that produces nearly monoenergetic beams with low angular divergence determined by the optics and curvature of the grids.

In the crossed electric and magnetic field region of the channel, the electrons move in the azimuthal direction due to the $\mathbf{E} \times \mathbf{B}$ force with a velocity given by Eq. (3.3-16). The magnitude of the azimuthal electron velocity was found in Chapter 3 to be

$$v_E = \frac{\mathbf{E} \times \mathbf{B}}{B^2} \approx \frac{E_r}{B_z} \quad [\mathrm{m/s}]. \tag{7.2-4}$$

The current in the azimuthal direction, called the Hall current, is then the integral of the electron plasma density and this velocity over the characteristic thickness L [3,4]:

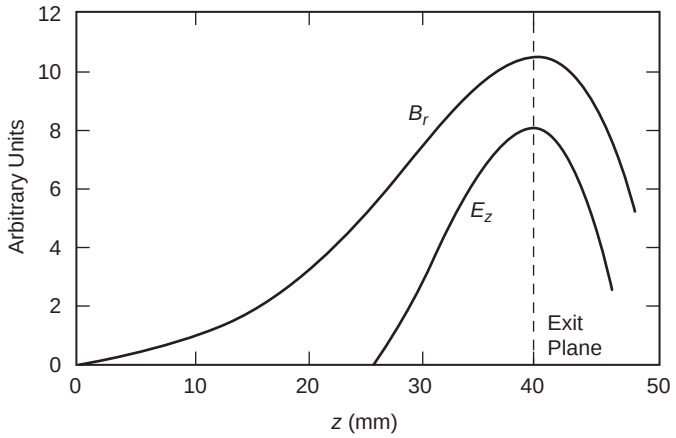

Fig. 7-6. Typical Hall thruster radial magnetic field and axial electric field along the channel length.

$$I_H = n_e e\left(\int_0^L v_E \, dz\right) w = n_e e\left(\int_0^L \frac{E}{B} dz\right) w, \tag{7.2-5}$$

where w is the plasma width (shown in Fig. 7-5) that essentially fills the channel. The axial electric field in the plasma channel is, approximately, the discharge voltage divided by the plasma thickness, so the Hall current is

$$I_H \approx n_e e w \frac{V_d}{B}. \tag{7.2-6}$$

Equation (7.2-6) shows that the Hall current increases with the applied discharge voltage and with the channel width provided that the magnetic field is unchanged. Hofer [10] showed that in Hall thrusters optimized for high efficiency, the optimal magnetic field was proportional to the discharge voltage. This implies that the Hall current is approximately constant for a given plasma density or beam current in high-efficiency Hall thrusters.

The ion current leaving the plasma to form the beam through the area A_e is approximately

$$I_i = n_i e v_i A_e \approx n_i e \sqrt{\frac{2eV_d}{M}} 2\pi R w, \tag{7.2-7}$$

where R is the average radius of the plasma channel. Since the plasma is quasi-neutral ($n_i \approx n_e$), even in the magnetized region, the Hall current can be expressed using Eq. (7.2-7) as

$$I_H \approx \frac{I_i}{2\pi R B} \sqrt{\frac{MV_d}{2e}}. \tag{7.2-8}$$

Increasing the beam current in a fixed thruster design will increase the circulating Hall current for a given magnetic field and discharge voltage. From Chapter 2, the total thrust produced by a Hall thruster is

$$T = \int \left(\mathbf{J}_H \times \mathbf{B}\right) dA = I_H B \approx I_i \sqrt{\frac{MV_d}{2e}}. \tag{7.2-9}$$

This expression for the thrust has the same form as Eq. (2.3-8) derived in Chapter 2, where the force is coupled magnetically to the Hall thruster body instead of electrostatically to the ion thruster grids.

7.2.2 Ionization Length and Scaling

It is clear from the description of the Hall thruster operation above that the electrons must be magnetized to reduce their axial mobility to the anode, but the ions cannot be significantly magnetized so that the axial electric field can efficiently accelerate them to form the thrust beam. In addition, a large majority of the ions must be generated in the channel to permit acceleration by the field in that region and to produce high mass utilization efficiency [13]. This provides some simple scaling rules to be established.

The neutral gas injected from the anode region will be ionized by entering the plasma discharge in the crossed-field "ionization" region. Consider a neutral gas atom at a velocity v_n incident on plasma of a density n_e, electron temperature T_e, and thickness L. The density of the neutral gas will decrease with time due to ionization:

$$\frac{dn_n}{dt} = -n_n n_e \langle \sigma_i v_e \rangle, \tag{7.2-10}$$

where $\langle \sigma_i v_e \rangle$ is the ionization reaction rate coefficient for Maxwellian electrons, described in Appendix E. The flux of neutrals incident on the plasma is

$$\Gamma_n = n_n v_n, \tag{7.2-11}$$

and the neutral velocity is $v_n = dz/dt$, where z is the axial length. Equation (7.2-10) then becomes

$$\frac{d\Gamma_n}{\Gamma_n} = -\frac{n_e \langle \sigma_i v_e \rangle}{v_n} dz. \tag{7.2-12}$$

This equation has a solution of

$$\Gamma_n(z) = \Gamma(0) e^{-z/\lambda_i}, \tag{7.2-13}$$

where $\Gamma(0)$ is the incident flux on the ionization region and the ionization mean free path λ_i is given by

$$\lambda_i = \frac{v_n}{n_e \langle \sigma_i v_e \rangle}. \tag{7.2-14}$$

This expression for the ionization mean free path is different from the usual one, given in Eq. (3.6-6), that applies for the case of fast particles incident on essentially stationary particles. This is because the neutral gas atoms are moving slowly as they traverse the plasma thickness, and the fast electrons can move laterally to produce an ionization collision before the neutral leaves the region. Therefore, the ionization mean-free path depends on the neutral velocity, which determines the time the atom spends in the plasma thickness prior to a collision. The mean-free path also varies inversely with the electron density because a higher number of electrons in the slab will increase the probability of one of them encountering the neutral atom.

The percentage of the neutrals exiting the plasma of length L that are ionized is

$$\frac{\Gamma_{\text{exit}}}{\Gamma_{\text{incident}}} = 1 - e^{-L/\lambda_i} . \tag{7.2-15}$$

For example, in order to have 95% of the incident neutral flux on the plasma ionized before it leaves the plasma, Eq. (7.2-15) gives

$$L = -\lambda_i \ln(1-.95) = 2.996\lambda_i = \frac{3\nu_n}{n_e\langle\sigma_i v_e\rangle}, \tag{7.2-16}$$

or the plasma thickness must be at least three times the ionization mean-free path. Since some of the ions generated in the plasma hit the channel side walls and re-enter the plasma as neutrals instead of exiting as beam ions, the plasma thickness should significantly exceed the ionization mean-free path to obtain high mass utilization efficiency. This leads to one of the Hall thruster scaling rules:

$$\frac{\lambda_i}{L} = \text{constant} << 1. \tag{7.2-17}$$

In this example, this ratio should be less than 0.33.

The actual channel's physical depth in dielectric-wall Hall thrusters is given by the sum of the magnetized plasma thickness (L) and the geometric length required to demagnetize the plasma at the anode. This is illustrated schematically in Fig. 7-6, where the channel depth is nearly twice the magnetized plasma length. The axial magnetic field gradient has been found to be critical for the thruster performance [12]. A decreasing radial magnetic field strength going toward the anode, as shown in Fig. 7-6, results in higher thruster efficiency [4,12]. At the anode, the plasma is largely unmagnetized, and an anode sheath forms to maintain particle balance, similar to the DC plasma

generator case discussed in Chapter 4. The anode sheath polarity and magnitude depend on the local magnetic field strength and direction, which affects the axial electron mobility, and on the presence of any insulating layers on the anode that affects the particle balance [14–16]. Maintaining the local plasma near the anode close to the anode potential is important in applying the maximum amount of the discharge voltage across the plasma for the acceleration of ions. In addition, the magnetic field profile near the thruster exit strongly affects both the ability to achieve closed electron drifts in the azimuthal direction [8] and the focusing of the ions in the axial direction as they are accelerated by the electric field [9]. Optimal magnetic field design in the exit region reduces the ion bombardment of the walls and improves the ion trajectories leaving the thruster [17].

Additional information on the thruster operation can be obtained by examining the ionization criteria. Properly designed Hall thrusters tend to ionize essentially all of the propellant gas incident on the plasma from the anode, so that

$$n_n n_e \langle \sigma_i v_e \rangle A_e L \approx n_n v_n A_e. \tag{7.2-18}$$

Using Eq. (7.2-6) for the Hall current, Eq. (7.2-18) becomes

$$L = \frac{v_n V_d w}{I_H \langle \sigma_i v_e \rangle B}. \tag{7.2-19}$$

The length of the ionization region naturally must increase with neutral velocity and can decrease with the ionization reaction rate coefficient, as seen in Eq. (7.2-16). This is important in order to achieve high mass utilization when propellants with a lower mass than xenon, such as krypton, are used to increase the Isp of the thruster [18,19].

Studies of optimized Hall thrusters of different sizes [20–25] have resulted in some scaling laws. A detailed comparison of the scaling laws in the literature, with experimental results from the family of empirically optimized stationary plasma thrusters (SPTs), was performed by Daren, et al. [20]. Assuming that the thruster channel inner-to-outer diameter ratio and the ionization mean-free path-to-plasma length ratio are constants, they found

$$\begin{aligned} &\text{power} \propto \text{thrust} \propto R^2 \\ &I_d \propto R^2 \\ &\dot{m} \propto R^2 \\ &w = R(1 - \text{constant}) \\ &A_e = \pi\left(R^2 - r^2\right), \end{aligned} \tag{7.2-20}$$

where R is the outside radius of the channel. These scaling rules indicate that the optimum current density is essentially constant as the thruster size changes. The current density in Hall thrusters is typically in the range of 0.1 to 0.15 A/cm^2. Thus, at a given discharge voltage, the power density in a Hall thruster is also constant. Higher power densities are achieved by increasing the voltage, which has implications for the life of the thruster.

7.2.3 Potential and Current Distributions

The electrical schematic for a Hall thruster is shown in Fig. 7-7. The power supplies are normally all connected to the same reference, called the *cathode common*. The hollow cathode requires the same power supplies as an ion thruster, namely, a heater supply to raise the emitter to thermionic emission temperatures and a keeper supply for ignition and to ensure stable cathode operation at very low currents. The discharge supply is connected between the cathode common (typically also connected to the thruster body or magnetic circuit) and the anode located in the bottom of the channel. As in ion thrusters, the cathode heater is turned off once the discharge supply is turned on, and the cathode runs in a self-heating mode. The keeper is also normally used only during start-up and is turned off once the thruster is ignited. Also shown are the inner and outer magnetic field coils and their associated power supplies. Hall thrusters have been built with the cathode positioned on-axis (not shown), but this does not change the electrical schematic.

The potential distribution in a Hall thruster [26] is also illustrated in Fig. 7-7. In the upstream region of the channel where the transverse magnetic field is low, the plasma is weakly magnetized and the electron mobility is high. The plasma potential is then close to the anode potential. The plasma potential decreases toward the cathode potential near the thruster exit plane as the magnetic field increases (shown in Fig. 7-6) and limits the electron mobility. The difference between the cathode potential and the beam potential is the coupling voltage V_c, which is the voltage required to extract current from the hollow cathode. The beam voltage is then

$$V_b = V_d - V_c. \tag{7.2-21}$$

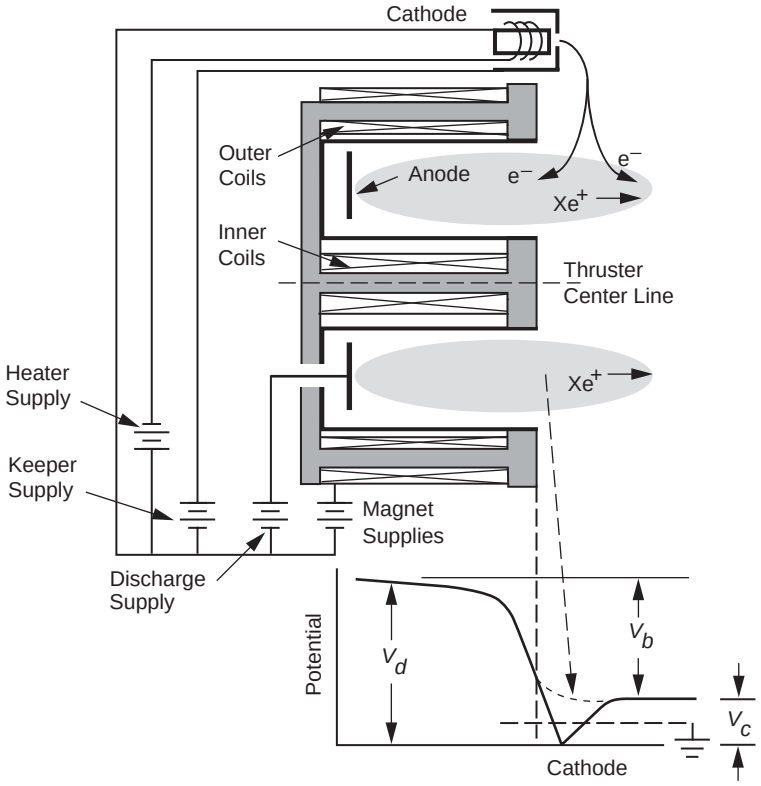

Fig. 7-7. Hall thruster electrical schematic and potential distribution.

It is common in laboratory experiments to sometimes ignore the difference in potential between the beam and ground as small (typically 10 to 20 V) and to write the beam voltage as

$$V_b \approx V_d - V_{cg}, \tag{7.2-22}$$

where V_{cg} is the cathode-to-ground voltage.

The on-axis potential, shown schematically by the dashed line in Fig. 7-7, decreases from the ionization and acceleration regions to the thrust-beam plasma potential. Ions are generated all along this potential gradient, which causes a spread in the ion energy in the beam. Since the majority of the ions are generated upstream of the exit plane (in the "ionization region"), the average velocity of the ion beam can then be expressed as

$$\langle v_b \rangle = \sqrt{\frac{2e\bar{V}_b}{M}}, \tag{7.2-23}$$

where $\bar{V}_b$ represents, in this case, the average potential across which the ions are accelerated. The actual spread in the beam energy can be significant [27,28] and must be measured by plasma diagnostics.

The beam from the Hall thruster is charge neutral (equal ion and electron currents). As in ion thrusters, the thruster floats with respect to either spacecraft common in space or vacuum-chamber common on the ground. The common potential normally floats between the cathode and the beam potentials and can be controlled on a spacecraft by a resistor between the spacecraft common and the cathode common. The actual beam energy cannot be measured directly across the power supplies because the potential difference between the beam and ground or spacecraft common is unknown and must be measured by probes or energy analyzers. The coupling voltage is typically on the order of 20 V in order to operate the cathode discharge properly, which usually ranges from 5% to 10% of the discharge voltage for Hall thrusters with moderate Isp.

In a Hall thruster, the measured discharge current is the net current flowing through the discharge supply. The current flowing in the connection between the anode and the power supply in Fig. 7-7 is the electron and ion current arriving to the anode:

$$I_d = I_{ea} - I_{ia}. \tag{7.2-24}$$

The ion current is typically small due to its higher mass, and so the discharge current is essentially the electron current collected by the anode. Likewise, the current flowing in the cathode leg (neglecting any keeper current) is

$$I_d = I_e + I_{ic}, \tag{7.2-25}$$

where I_e is the emitted current and I_{ic} is the ion current flowing back to the cathode. As with the anode, the ion current to the cathode is typically small, and so the discharge current is essentially just the cathode electron emission current. Therefore, the discharge current is approximately

$$I_d \approx I_e \approx I_{ea}. \tag{7.2-26}$$

Figure 7-8 shows a simplified picture of the currents flowing through the plasma, where the ion currents to the anode and cathode are neglected as small and the ion and electron currents to the dielectric walls are equal and are not shown. Ions are produced in the plasma by ionization events. The secondary electrons from the ionization events, I_{ei}, go to the anode, along with the primary electrons from the cathode, I_{ec}. Primary electrons either ionize neutrals or contribute energy to the plasma electrons so that the energetic

electron distribution can produce the ionization. Since it is assumed that the discharge current is essentially the total electron current collected by the anode (the ion current is small), the discharge current can be written as

$$I_d = I_{ei} + I_{ec}. \tag{7.2-27}$$

The discharge current is also essentially the electron current emitted by the cathode:

$$I_d = I_e = I_{ec} + I_{eb}. \tag{7.2-28}$$

Using the fact that one electron and one ion are made in each ionization event such that $I_{ei} = I_{ib}$, Eq. (7.2-27) becomes

$$I_d = I_{ib} + I_{ec}. \tag{7.2-29}$$

This relationship describes the net current crossing the exit plane, and so it is commonly stated in the literature that the discharge current is the ion beam current plus the backstreaming electron current crossing the exit plane [4,9].

Depending on the plasma conditions, it is possible for some fraction of the secondary electrons produced near the channel exit to diffuse into the beam. Equation (7.2-29) is still valid in this case because for every secondary electron that diffuses into the beam, another electron from the cathode plasma must cross the exit plane in the opposite direction to maintain the net discharge current. The discharge current is still the net ion beam current plus the backstreaming electron current across the exit plane. Finally, the ion beam current is equal to the current of electrons entering the beam:

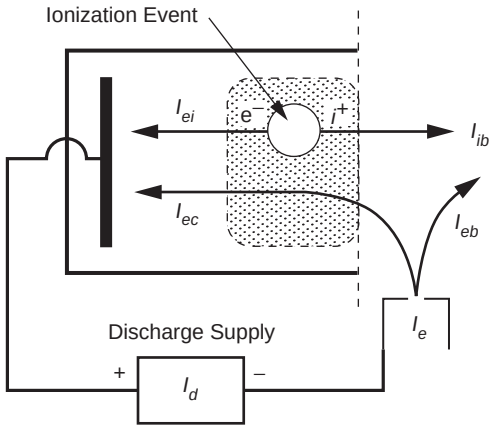

Fig. 7-8. Electrical schematic for the currents flowing through the discharge plasma and power supply.

$$I_{ib} = I_{eb}. \tag{7.2-30}$$

Since there is no current return path for the beam ions and electrons because the thruster floats relative to the spacecraft or the grounded vacuum system, the particles in Eq. (7.2-30) do not directly contribute to the discharge current measured in the discharge power supply.

7.3 Hall Thruster Performance Models

The efficiency of a generic electric thruster was derived in Chapter 2. Since the beam current and ion energy in Hall thrusters are not directly measured as in ion thrusters, it is useful to develop an alternative expression for the efficiency that incorporates characteristics of Hall thruster discharges. Total efficiency is always defined as the jet power, which is the thrust times the exhaust velocity, divided by the total input power:

$$\eta_T = \frac{T \ v}{P_{\text{in}}}. \tag{7.3-1}$$

For any electric thruster, the exhaust velocity is given by Eq. (2.3-6), the Isp is given by Eq. (2.4-1), and the thrust is given by Eq. (2.3-1), which can be combined to give

$$v = \frac{\text{Isp} \cdot g}{2} = \frac{g}{2}\frac{v}{g}\frac{\dot{m}_i}{\dot{m}_p} = \frac{1}{2}\frac{T}{\dot{m}_p}. \tag{7.3-2}$$

The total efficiency is then

$$\eta_T = \frac{T^2}{2\dot{m}_p P_{\text{in}}}. \tag{7.3-3}$$

7.3.1 Hall Thruster Efficiency

In Hall thrusters, the gas flow is split between the anode inside the discharge channel and the hollow cathode:

$$\dot{m}_p = \dot{m}_a + \dot{m}_c, \tag{7.3-4}$$

where $\dot{m}_a$ is the anode flow rate and $\dot{m}_c$ is the cathode flow rate.

Since the cathode gas flow is injected exterior to the discharge channel ionization region and is, thereby, largely lost, the “cathode efficiency” is defined as

$$\eta_c = \frac{\dot{m}_a}{\dot{m}_p} = \frac{\dot{m}_a}{\dot{m}_a + \dot{m}_c}. \tag{7.3-5}$$

The total power into the thruster is

$$P_{\text{in}} = P_d + P_k + P_{\text{mag}}, \tag{7.3-6}$$

where P_d is the discharge power, P_k is the cathode keeper power (normally equal to zero during operation), and P_{mag} is the power used to generate the magnetic field. The electrical utilization efficiency for the other power used in the Hall thruster is defined as

$$\eta_o = \frac{P_d}{P_T} = \frac{P_d}{P_d + P_k + P_{\text{mag}}}. \tag{7.3-7}$$

Using Eqs. (7.3-5) and (7.3-7) in Eq. (7.3-3) gives a useful expression for the total efficiency of a Hall thruster:

$$\eta_T = \frac{1}{2}\frac{T^2}{\dot{m}_a P_d}\eta_c \eta_o. \tag{7.3-8}$$

By placing the Hall thruster on a thrust stand to directly measure the thrust, knowing the flow rates and flow split between anode and cathode, and knowing the total power into the discharge, keeper, and magnet, it is then possible to accurately calculate the total efficiency.

While Eq. (7.3-8) provides a useful expression for evaluating the efficiency, it is worthwhile to further expand this equation to examine other terms that affect the efficiency. Thrust is given from Eq. (2.3-16):

$$T = \gamma \sqrt{\frac{2M}{e}}\, I_b \, \sqrt{\bar{V}_b}\,, \tag{7.3-9}$$

where the average or effective beam voltage is used due to the spread in ion energies produced in the Hall thruster acceleration region. The fraction of the discharge current that produces beam current is

$$\eta_b = \frac{I_b}{I_d}. \tag{7.3-10}$$

Likewise, the fraction of the discharge voltage that becomes beam voltage is

$$\eta_v = \frac{V_b}{V_d}. \tag{7.3-11}$$

Inserting Eqs. (7.3-9) through (7.3-11) into Eq. (7.3-8) gives

$$\eta_T = \gamma^2 \frac{M}{e} \frac{I_d}{\dot{m}_a} \eta_b^2 \eta_v \eta_c \eta_o. \tag{7.3-12}$$

Equation (7.3-12) shows that the Hall thruster efficiency is proportional to the ion mass and the discharge current, because these terms dominate the thrust production, and is inversely proportional to the anode mass flow, which dominates the mass utilization efficiency. This equation can be further simplified by realizing that

$$\frac{M}{e} I_d \eta_b = \dot{m}_i, \tag{7.3-13}$$

and that the total mass utilization efficiency can be expressed as

$$\eta_m = \frac{\dot{m}_i}{\dot{m}_p} = \frac{\dot{m}_i}{\dot{m}_a + \dot{m}_c}. \tag{7.3-14}$$

The total efficiency then becomes

$$\eta_T = \gamma^2 \eta_b \eta_v \eta_m \eta_o. \tag{7.3-15}$$

This expression contains the usual gamma-squared term associated with beam divergence and multiply charged ion content and also the mass utilization and electrical utilization efficiencies. However, this expression also includes the efficiencies associated with generating beam ions and imparting the discharge voltage to the beam voltage. This shows directly that Hall thruster designs that maximize beam current production and beam energy and that minimize the cathode flow produce the maximum efficiency, provided that the beam divergence and double-ion content are not adversely affected. Expressions like Eq. (7-3-15) appear in the Hall thruster literature [4,7] because they are useful in illustrating how the efficiency depends on the degree to which the thruster converts power supply inputs (such as discharge current and voltage) into the beam current and beam voltage that impart thrust. Understanding each efficiency term is critical to fully optimizing the Hall thruster performance.

The efficiency of a Hall thruster is sometimes expressed in terms of the anode efficiency:

$$\eta_a = \frac{1}{2}\frac{T^2}{\dot{m}_a P_d} = \frac{\eta_T}{\eta_o \eta_c}, \qquad (7.3\text{-}16)$$

which describes the basic thruster performance without considering the effects of the cathode flow or power used to generate the magnetic field. This is usually done to separate out the cathode and magnet losses so that trends in the plasma production and acceleration mechanisms can be discerned. The anode efficiency should not be confused with the total efficiency of the thruster given by Eq. (7.3-3).

It is useful to show an example of the relative magnitude of the efficiency terms derived above. Figure 7-9 (from [10]) shows the anode efficiency that was defined in Eq. (7.3-16) and the other efficiency terms discussed above for the laboratory-model NASA-173Mv2 Hall thruster operating at 10 mg/s versus the discharge voltage. In this figure, the charge utilization efficiency is the net efficiency decrease due to multiply charged ions [10], the voltage utilization efficiency (η_v) is the conversion of voltage into axially directed ion velocity, the current utilization efficiency (η_b) is the fraction of ion current contained in the discharge current, and mass utilization efficiency (η_m) is the conversion of neutral mass flux into ion mass flux. The anode efficiency increases with discharge voltage, largely because the voltage efficiency and current efficiency increase with voltage. The current utilization is always lower than the other efficiency terms, suggesting that the ultimate efficiency of Hall thrusters is dominated by the electron dynamics involved in producing the plasma and neutralizing the beam. This emphasizes the importance [9,10] of optimizing the magnetic field design to maximize the thruster efficiency.

The value of γ in Eq. (7.3-15) that is typically found for Hall thrusters can be evaluated using Eq. (2.3-15) and the data in the literature. For example, a 10% double-ion content gives a thruster correction factor in Eq. (2.3-14) of $\alpha = 0.973$. The thrust loss due to the beam angular divergence of Hall thrusters is given by Eq. (2.3-10), ($F_T = \cos\theta$). For both SPT-100 Hall thrusters [6] and TAL thrusters [29], a half-angle divergence of θ equal to about 20~deg is observed, producing $F_T = 0.94$. The total correction factor is then $\gamma = \alpha F_T = 0.915$ for typical Hall thruster conditions. Values for γ of about 0.9 have been reported.

The equivalent discharge loss for a Hall thruster can also be calculated [4,6] to provide information on how the thruster design impacts the cost of producing the beam ions. The average energy cost for producing a beam ion is the

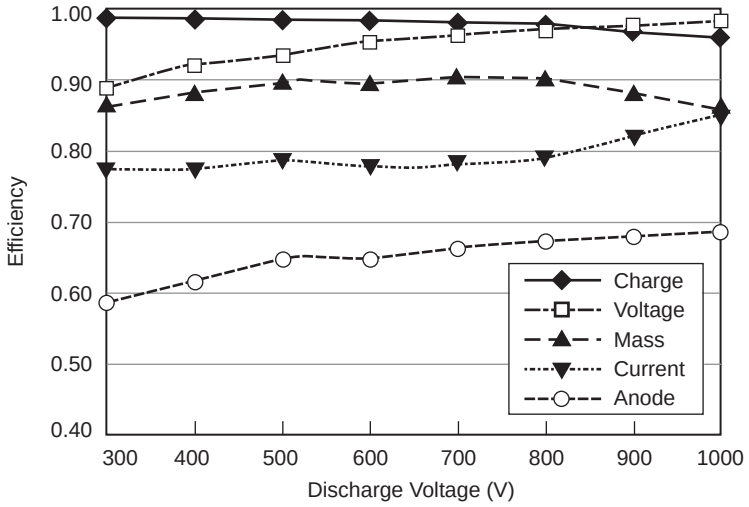

Fig. 7-9. Optimized anode efficiency and the individual efficiency terms versus discharge voltage for the NASA-173Mv2 Hall thruster operating at 10 mg/s (from [10]).

discharge power divided by the number of beam ions minus the beam power per beam ion:

$$\varepsilon_b = \frac{I_d V_d}{I_b} - \frac{I_b V_b}{I_b} = \frac{I_d V_d}{I_b} - V_b = \frac{P_d\left(1-\eta_b\eta_v\right)}{I_b}, \qquad (7.3\text{-}17)$$

where Eqs. (7.3-10) and (7.3-11) were used. Equation (7.3-17) has the usual units for discharge loss of watts per beam-amp or electron-volts per ion. As expected, maximizing the current and voltage efficiencies minimizes the discharge loss. As an example of discharge loss in a Hall thruster, consider the SPT-100 thruster operating at the nominal 1.35-kW discharge power and 300 V. The discharge current is then 1350/300 = 4.5 A. The thruster is reported [4–6] to have values of $\eta_b \approx 0.7$ and $\eta_v = 0.95$. The cost of producing beam ions is then

$$\varepsilon_b = \frac{P_d\left(1-\eta_b\eta_v\right)}{I_b} = \frac{1350\left(1-0.7*0.95\right)}{0.7*4.5} = 144 \text{ [eV/ion]}.$$

This is on the same order as the discharge loss for DC-discharge ion thrusters.

7.3.2 Multiply Charged Ion Correction

In Hall thrusters operating at higher power levels (high mass flow rate and high discharge voltages >300 V), a significant number of multiply charged ions can

be generated, and their effect on the performance may be noticeable. Following the analysis by Hofer [11], the performance model from the previous section can be modified to address the case of partially ionized thruster plasmas with an arbitrary number of ion species.

The total ion beam current is the sum of each ion species *i*:

$$I_b = \sum_{i=1}^{N} I_i \ . \tag{7.3-18}$$

The current fraction of the *i*th species is

$$f_i = \frac{I_i}{I_b}. \tag{7.3-19}$$

Likewise, the total plasma density in the beam is the sum of the individual species densities,

$$n_b = \sum_{i=1}^{N} n_i \ , \tag{7.3-20}$$

and the density fraction of the *i*th species is

$$\zeta_i = \frac{n_i}{n_b}. \tag{7.3-21}$$

The total beam current is then

$$I_b = \sum_i n_i q_i \langle v_i \rangle A_e = \sum_i n_b e \sqrt{\frac{2eV_b}{M}} \zeta_i Z_i^{3/2} \ , \tag{7.3-22}$$

where Z_i is the charge state of each species. The mass flow rate of all the beam ion species is

$$\dot{m}_b = \frac{I_b M}{e} \sum_i \frac{f_i}{Z_i} \ . \tag{7.3-23}$$

Using the current utilization efficiency defined in Eq. (7.3-10), the mass utilization efficiency in Eq. (7.3-14) then becomes

$$\eta_m = \frac{\dot{m}_b}{\dot{m}_p} = \frac{\eta_b I_d M}{\dot{m}_p e} \sum_i \frac{f_i}{Z_i} . \tag{7.3-24}$$

If the current utilization efficiency is the same for each species, then the mass utilization efficiency for arbitrary species can be written as

$$\eta_m = \eta_m^+ \sum_i \frac{f_i}{Z_i} , \tag{7.3-25}$$

where η_m^+ is the usual mass utilization for a singly charged species. This is an easily implemented correction in most models if the species fractions are known. Likewise, the thrust obtained for multiple species can be generalized from Eq. (2.3-16) for Hall thrusters to

$$T_m = \sum_i T_i = \eta_b I_d \sqrt{\frac{2M\eta_b V_d}{e}} \sum_i \frac{f_i}{Z_i} \cos\theta. \tag{7.3-26}$$

7.3.3 Dominant Power Loss Mechanisms

In preparation for examining the terms that drive the efficiency of Hall thrusters, it is useful to examine the dominant power-loss mechanisms in the thruster. Globally, the power into the thruster comes from the discharge power supply. The power out of the thruster, which is equal to the input power, is given to first order by

$$P_d = P_b + P_w + P_a + P_R + P_{\text{ion}} , \tag{7.3-27}$$

where P_b is the beam power given by $I_b V_b$, P_w is the power to the channel walls due to ion and electron loss, P_a is the power to the anode due to electron collection, P_R is the radiative power loss from the plasma, and P_{ion} is the power to produce the ions that hit the walls and become the beam. Additional loss terms, such as the power that electrons take into the beam, the ion power to the anode, etc., are relatively small and can usually be neglected.

In Hall thrusters with dielectric walls, the power loss due to electron and ion currents flowing along the radial magnetic field through the sheath to the channel walls (P_w) represents the most significant power loss. The current deposition and power lost to the walls can be estimated from the sheath potentials and electric fields in the plasma edge. Since the wall is insulating, the net ion and electron currents to the surface must be equal. However, ion and electron bombardment of common insulator materials, such as boron nitride, at

the energies characteristic of Hall thrusters produces a significant number of secondary electrons, which reduces the sheath potential at the wall and increases the power loading.

The requirement of local net current equal to zero and particle balance for the three species gives

$$I_{iw} = I_{ew} - \gamma I_{ew} = I_{ew}\left(1-\gamma\right), \tag{7.3-28}$$

where γ is the secondary electron yield from electron bombardment. Using Eq. (3.7-51) for the Bohm current of ions to the wall, Eq. (3.7-52) for the electron current to the wall, and neglecting the secondary electron velocity, Eq. (7.3-28) can be solved for the sheath potential ϕ_s, including the effect of secondary electron emission:

$$\phi_s = \frac{kT_e}{e}\ln\left[\left(1-\gamma\right)\sqrt{\frac{2M}{\pi m}}\right]. \tag{7.3-29}$$

This expression is slightly different than that found in the literature [30,31] because we have approximated $e^{-1/2} = 0.61 \approx 0.5$ for the coefficient in the expression for the Bohm current. Nevertheless, as the secondary electron yield increases, the sheath potential decreases from the classic floating potential described in Chapter 3 toward the plasma potential.

Secondary electron yields reported in the literature [30,32,33] for several materials used for the walls of Hall thrusters are shown in Fig. 7-10. In this figure, the measurements were made using a monoenergetic electron gun. Generalizing these data for incident Maxwellian electron temperatures is accomplished by integrating the yield over the Maxwellian electron energy distribution function, which results in multiplying the secondary emission scaling by the gamma function [30]. An expression for the secondary electron yield from electron bombardment of materials is then

$$\gamma = \Gamma(2+b)aT_{\mathrm{eV}}^{b}, \tag{7.3-30}$$

where the electron temperature is in electron volts, $\Gamma(x)$ is the gamma function, and the coefficients a and b are found from fits to the data in Fig. 7-10. Values of the coefficients in Eq. (7.3-30) can be found in Table 7-1 for these materials, and the actual secondary electron yield for the Hall thruster walls is plotted versus plasma electron temperature in Fig. 7-11. It should be noted that due to reflection at the wall, the effective secondary electron yield does not go to zero for zero electron energy. This effect is accommodated by linear fits to the data

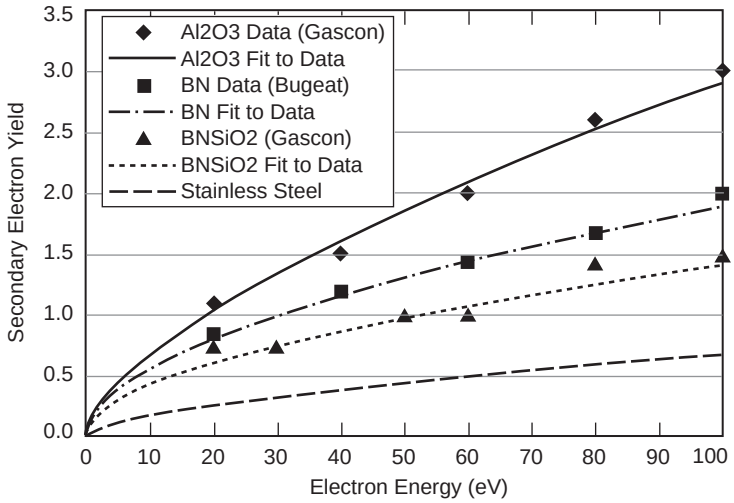

Fig. 7-10. Secondary electron yield for several wall materials used in Hall thrusters, measured with a mono-energetic electron beam.

Table 7-1. Fitting parameters for secondary electron yield data.

	a	**b**	$\Gamma(2 + b)$
Alumina (Al_2O_3)	0.145	0.650	1.49
Boron Nitride (BN)	0.150	0.549	1.38
$BNSiO_2$	0.123	0.528	1.36
Stainless steel	0.040	0.610	1.44

that result in finite yield at low electron energy. Figure 7-12 shows the data for boron nitride and $BNSiO_2$ with the two different fitting choices. In the evaluation of the sheath potential in the presence of the secondary electron emission below, whether one uses a linear or power fit does not make a significant difference in the ionization and acceleration regions for electron temperatures above about 10 eV.

Measurements of the electron temperature in the channel of Hall thrusters by a number of authors [34–36] show electron temperatures in the channel well in excess of 20 eV. Equation (7.3-29) predicts that the sheath potential will go to zero and reverse from negative going (electron repelling) to positive going (electron attracting) as the secondary electron yield approaches unity for some of the materials. The value at which this occurs for each of the materials shown in Table 7-1 is indicated in Fig. 7-11. For boron nitride and alumina walls this occurs at electron temperatures below 20 eV, and for BN-SiO_2 walls it occurs at

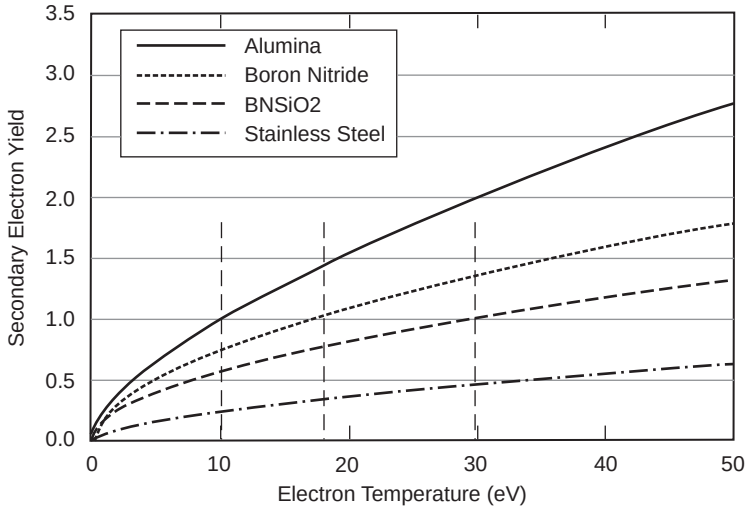

Fig, 7-11. Secondary electron yield from the power-curve fits versus electron temperature, showing the cross-over value at which the yield equals one.

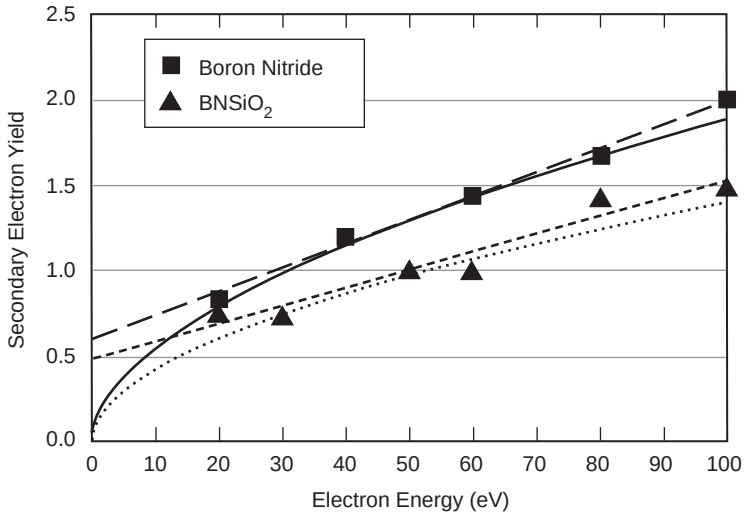

Fig. 7-12. Secondary electron yield versus electron energy, showing linear curve fits to the data producing finite yield at low incident energy.

electron temperatures on the order of 30 eV. In addition, depending on the collision mean-free path, some of the secondary electrons can pass completely through the plasma to strike the opposite wall of the channel. The possibility of the sheath potential reversing to electron attracting was used to predict very high electron power losses to the walls in some early analyses of Hall thrusters

at high electron temperatures [30,31] because the incident electron flux can then equal or exceed the random electron flux along the magnetic field lines in the plasma.

In reality, the sheath potential for a floating boundary can never go significantly more positive than the local plasma potential [37,38] for two reasons. First, the secondary electrons are ejected from the wall with very low energy (typically 1–2 eV). Any positive-going sheath (where the plasma is negative by one or two volts relative to the wall) will repel the secondary electrons and return them to the wall. This clamps the sheath potential to within a few volts positive with respect to the plasma. Second, the secondary electron emission is space charge–limited in the sheath. This effect was analyzed by Hobbs and Wesson [39], who showed that space charge limits the secondary electron current from the wall independently of the secondary electron yield. The local electron space charge in the sheath clamps the sheath voltage to a maximum value that is always negative relative to the plasma.

The effects of space charge on the sheath potential at the wall can be analyzed [39] by solving Poisson's equation for the potential in the sheath:

$$\frac{\partial^2 \phi}{\partial x^2} = \frac{1}{\varepsilon_o}\left(n_e + n_s - n_i\right), \tag{7.3-31}$$

where n_s is the secondary electron density. Using a Maxwellian distribution for the electrons, the plasma density in the channel is

$$n_e = \left(n_o - n_{so}\right) e^{e\phi/kT}, \tag{7.3-32}$$

where n_o is the ion density at the sheath edge, n_{so} is the secondary electron density at the sheath edge, and ϕ is the potential relative to the potential ϕ_o at the wall. The ions are assumed to be cold and to have fallen through the pre-sheath to arrive at the sheath edge with an energy of

$$\mathcal{E} = \frac{1}{2} m v_o^2, \tag{7.3-33}$$

where v_o is the Bohm velocity modified for the presence of the secondary electrons. The ion density through the sheath is then

$$n_i = n_o \left(\frac{\mathcal{E}}{\mathcal{E} - e\phi} \right)^{1/2}. \tag{7.3-34}$$

The secondary electrons are assumed to be emitted with an energy that is small compared to the plasma electron temperature and are accelerated through the sheath. The equation of continuity for current at the sheath edge gives

$$n_s v_s = \frac{\gamma}{1-\gamma} n_o v_o, \tag{7.3-35}$$

where v_s is the secondary electron velocity. The secondary electron density through the sheath is then

$$n_s = n_o \frac{\gamma}{1-\gamma}\left(\frac{m}{M}\frac{\mathcal{E}}{\phi-\phi_o}\right). \tag{7.3-36}$$

Equations (7.3-32), (7.3-34), and (7.3-36) are inserted into Poisson's equation, Eq. (7.3-31), and evaluated by the usual method of multiplying through by $d\phi/dx$ and integrating to produce

$$\begin{aligned}\frac{1}{2\varepsilon_o n_o kT_e}\left(\frac{d\phi}{dx}\right)^2 = {} & \frac{2\mathcal{E}}{kT_e}\left[\left(1-\frac{e\phi}{\mathcal{E}}\right)^{1/2}-1\right] \\ & + \frac{2\gamma}{1-\gamma}\left(-\frac{m}{M}\frac{\mathcal{E}}{kT_e}\frac{e\phi_o}{kT_e}\right)^{1/2}\left[\left(1-\frac{\phi}{\phi_o}\right)^{1/2}-1\right] \\ & + \left[1-\frac{\gamma}{1-\gamma}\left(-\frac{m}{M}\frac{\mathcal{E}}{e\phi_o}\right)^{1/2}\right]\left[\exp\left(\frac{e\phi}{kT_e}\right)-1\right].\end{aligned} \tag{7.3-37}$$

A monotonic sheath potential is found [39] for

$$\mathcal{E} = \frac{kT_e}{2} + \frac{\gamma}{1-\gamma}\left(\frac{m}{M}\right)^{1/2}\left(\frac{-\mathcal{E}}{e\phi_o}\right)^{3/2}\left(\frac{kT_e}{2}-e\phi_o\right). \tag{7.3-38}$$

For the case of no secondary electron emission (γ going to zero), the Bohm criteria solution of $\mathcal{E} \geq kT_e/2e$ is recovered. Due to the large electron-to-ion mass ratio for xenon, the right-hand term is always small and the ion velocity at the sheath edge for the case of finite secondary electron emission will be near the Bohm velocity. Hobbs and Wesson evaluated this minimum ion energy at the sheath edge for the case of space charge–limited emission of electrons at the wall, $d\phi_o/dx = 0$ in Eq. (7.3-37), and they found

$$\mathcal{E}_o = 0.58 \frac{kT_e}{e}. \tag{7.3-39}$$

Equation (7.3-39) indicates that the Bohm sheath criterion will still approximately apply (within about 16%) in the presence of secondary electron emission.

The value of the sheath potential for the space charge–limited case can be found by setting the electric field at the wall equal to zero in Eq. (7.3-37) and evaluating the potential using Eq. (7.3-38) and the current continuity equation:

$$\frac{1}{4}\left[1 - \frac{\gamma}{1-\gamma}\left(-\frac{m}{M}\frac{\mathcal{E}}{e\phi_o}\right)^{1/2}\right]\exp\left(\frac{e\phi_o}{kT_e}\right)\left(\frac{8kT_e}{\pi m}\right)^{1/2} = \frac{1}{1-\gamma}\left(\frac{2\mathcal{E}}{M}\right)^{1/2}. \tag{7.3-40}$$

The space charge–limited sheath potential for xenon is found to be

$$\phi_o = -1.02 \frac{kT_e}{e}. \tag{7.3-41}$$

The secondary electron yield at which the sheath becomes space-charge limited [39] is approximately

$$\gamma_o = 1 - 8.3\left(\frac{m}{M}\right)^{1/2}, \tag{7.3-42}$$

which for xenon is 0.983.

This analysis shows that the sheath potential for a xenon plasma decreases from $-5.97T_e$ for walls where the secondary electron yield can be neglected to $-1.02T_e$ for the case of space charge–limited secondary electron emission that will occur at high plasma electron temperatures. The value of the sheath potential below the space-charge limit can be found exactly by evaluating the three equations, Eqs. (7.3-37), (7.3-38), and (7.3-40), for the three unknowns (ϕ, γ, and $\mathcal{E}$).

However, the value of the sheath potential relative to the plasma edge in the presence of the secondary electron emission can be estimated by evaluating Eq. (7.3-29) while accounting for each of three species [38]. Quasi-neutrality for the three species in the plasma edge dictates that $n_i = n_e + n_s$, where n_s is the secondary electron density, and the flux of secondary electrons is the

secondary electron yield times the flux of plasma electrons. Equating the ion flux to the net electron flux to the wall gives

$$I_{iw} = n_i e v_i A = I_{ew}(1-\gamma) = \frac{1}{4} n_e (1-\gamma) e \left(\frac{8kT_e}{\pi m} \right)^{1/2} A \exp\left(\frac{e\phi_s}{kT_e} \right), \quad (7.3\text{-}43)$$

where the ion and electron densities are evaluated at the sheath edge. The sheath potential ϕ_s relative to the plasma potential is then

$$\phi_s = -\frac{kT_e}{e} \ln\left[\sqrt{\frac{M}{2\pi m}} \frac{n_e}{n_e + n_s} \frac{v_B}{v_i} (1-\gamma) \right], \quad (7.3\text{-}44)$$

where v_i is the modified ion velocity at the sheath edge due to the presence of the secondary electrons and the ion density is the sum of the plasma and secondary electrons. This equation is useful up to the space charge–limited potential of $\phi_o = -1.02 T_{\mathrm{eV}}$ and provides good agreement with the results for xenon described above for $n_e v_B / n_i v_i \approx 0.5$. The sheath potential predicted by Eq. (7.3-44) is plotted in Fig. 7-13 for two wall materials. In the limit of no secondary electron emission ($\gamma = 0$), the classic value for the sheath floating potential is obtained from Eq. (3.7-53). Once the electron temperature is sufficiently high to produce a yield approaching and even exceeding one, then the space charge–limited case of $\phi_o = -1.02 T_{\mathrm{eV}}$ is obtained. In between, the sheath potential depends on the electron temperature and material of the wall. Without the space charge–limited sheath regime predicted by Hobbs and Wesson, the potential would have continued along the thin dashed lines for the two cases and incorrectly resulted in very low sheath potentials and high power loadings at the wall.

The total power to the wall of the Hall thruster is

$$P_w = \frac{1}{4} \left(\frac{8kT_e}{\pi m} \right)^{1/2} e n_o A e^{e\phi_s / kT_e} \left(2 \frac{kT_e}{e} \right) + n_o e v_o A (\varepsilon - \phi_s), \quad (7.3\text{-}45)$$

where the first term is due to electrons overcoming the repelling sheath potential and depositing $2T_e$ on the wall, and the second term is due to ions that have fallen through the pre-sheath potential and then the full sheath potential. Note that n_o in this equation is the plasma density at the sheath edge and is roughly half the average plasma density in the center of the channel due to the radial pre-sheath. The cooling of the wall by the secondary electron

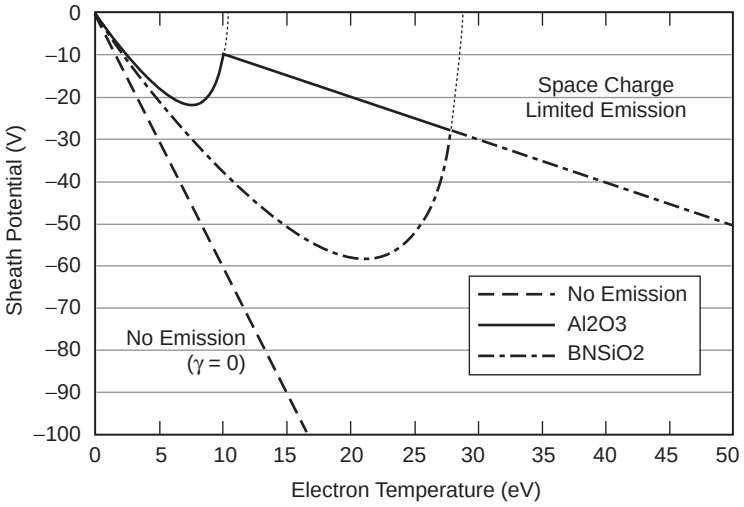

Fig. 7-13. Sheath potential versus electron temperature for two materials. The sheath transitions to space-charge limited where the dashed lines intersect the potential curves.

emission has been neglected. Equation (7.3-45) can be rewritten in terms of the total ion current to the wall as

$$P_w = I_{iw}\left[\left(\frac{M}{2\pi m}\right)^{1/2} e^{e\phi_s/kT_e}\left(2\frac{kT_e}{e}\right)+\left(\mathcal{E}-\phi_s\right)\right]. \qquad (7.3\text{-}46)$$

For the case of space charge–limited secondary electron emission, the sheath potential is $\phi_s = \phi_o = -1.02T_{\mathrm{eV}}$, and the ion energy is $\mathcal{E} = 0.58\,T_{\mathrm{eV}}$ in order to satisfy the Bohm condition. Equation (7.3-45) predicts the maximum heat loading to the wall in the presence of a Maxwellian electron distribution and secondary electron emission from the wall, which is the dominant power loss mechanism in dielectric-wall Hall thrusters. If the electron distribution function is non-Maxwellian, the heat load to the wall can differ from that predicted by Eq. (7.3-45).

In the case of TAL thrusters, the channel wall is metallic and biased to the cathode potential. This eliminates the zero-net current condition found on the insulating walls of dielectric-channel Hall thrusters and used to determine the local heat flux in Eq. (7.3-45). The electron flux to the cathode-biased TAL channel wall is negligible, and the secondary yield for metals is much lower than for insulators, so the secondary electron emission by the wall in TAL thrusters has little effect on the thruster operation. In addition, the plasma tends to be localized near the channel center by the anode design and gas feed geometry. The plasma then tends to be in poor contact with the guard rings at

the wall that also have a small exposed area to the plasma, resulting in low radial ion currents to the wall. This is evidenced by the erosion pattern typically observed on TAL guard rings [29], which tends to be on the downstream face from particles outside the thruster instead of on the inside diameter from the channel plasma. While the ion and electron currents and power deposition to the inside diameter of the metallic guard ring are likely smaller than in the dielectric-wall thruster case (where the power loss due to the electrons is dominant), the erosion on the face of the guard ring indicates energetic ion bombardment is occurring. This effect is significant in determining the life of the TAL.

However, TAL thrusters are characterized by having the anode in close contact with the magnetized plasma near the channel exit, in contrast to the dielectric-wall Hall thrusters. The magnetized plasma has a high electron temperature, which causes a significant amount of power to be deposited from the discharge current on the anode. It is possible to evaluate this power loss mechanism based on the current and sheath potential at the anode.

As described above, the discharge current is essentially equal to the electron current collected at the anode. In order for the TAL thruster to transfer a large fraction of the discharge voltage to the ions, the potential of the plasma near the anode must be close to the anode potential. Assuming the local plasma potential is then equal to or slightly positive relative to the anode, the electron current to the anode, I_a, deposits $2T_{\mathrm{eV}}$ in energy from the plasma (see Appendix C). The power deposited on the anode, P_a, is then given by

$$P_a = 2T_{\mathrm{eV}} I_a \approx 2T_{\mathrm{eV}} I_d , \tag{7.3-47}$$

where Eq. (7.2-26) has been used. If the plasma potential is negative relative to the anode, the thruster efficiency will suffer due to the loss of discharge voltage available to the ions, and the anode heating will increase due to the positive-going sheath potential accelerating electrons into the anode. Equation (7.3-47) then represents a reasonable, but not worst-case, heat flux to the anode.

This power loss to the anode can be related to the beam current using the fraction of the discharge current that produces beam current, which is defined as

$$\eta_b = \frac{I_b}{I_d} . \tag{7.3-48}$$

Therefore, the power to the anode is

$$P_a = 2T_{\mathrm{eV}} \frac{I_b}{\eta_b}. \tag{7.3-49}$$

In well-designed Hall thrusters, η_b ranges typically from 0.6 to 0.8. Therefore, the power loss to the anode is 3 to 4 times the product of the electron temperature in the near-anode region and the beam current. This is the most significant power loss mechanism in TAL thrusters.

7.3.4 Plasma Electron Temperature

The electron temperature in the channel must be known to evaluate the power loss mechanisms described above. The peak electron temperature in the plasma channel can be found using power balance, described by Eq. (7.3-27). This method provides reasonable estimates because the power loss in the thruster will be shown to be a strong function of the electron temperature. Even though the plasma density and electron temperature peak in different locations along the channel associated with the different ionization and acceleration regions, the strong axial electron temperature profile in Hall thrusters causes the majority of the power loss to occur in the region of the highest electron temperature. This occurs near the channel exit where the magnetic field across the channel is the strongest. Evaluating the plasma parameters and loss terms in this region, which is bounded by the channel width and magnetic axial field extent in the channel, establishes the electron temperature that is required to satisfy the power balance in the plasma for a given thruster current and voltage.

The individual terms in Eq. (7.3-27) will now be evaluated. The input power to the thruster is the discharge current times the discharge voltage ($P_d = I_d V_d$). The power in the beam, using Eq. (7.3-48), is

$$P_b = \eta_b \eta_v I_d V_d = \eta_v I_b V_d, \tag{7.3-50}$$

where the current utilization and voltage utilization efficiencies have to be known or evaluated by some means. The difference between the beam power and the discharge power is the power remaining in the plasma channel to produce the plasma and offset the losses:

$$P_p = (1-\eta_b) I_d V_d = I_{ec} V_d, \tag{7.3-51}$$

where P_p is the power into the plasma. The plasma is produced and heated essentially by the collisional transport of the electrons flowing from the cathode plasma in the near-plume region to the anode inside the thruster. The power into channel walls, from Eq. (7.3-45), can be written as

$$P_w = n_e eA\left[\frac{kT_e}{e}\left(\frac{kT_e}{2\pi m}\right)^{1/2} e^{e\phi_s/kT_e} + \frac{\nu_i}{2}\left(\mathcal{E} - \phi_s\right)\right], \qquad (7.3\text{-}52)$$

where A is the total area of the inner and outer channel walls in contact with the high temperature plasma region, ν_i is the ion velocity toward the wall, and the sheath potential ϕ_s is given by Eq. (7.3-44). Equation (7.3-52) shows the wall power varies linearly with density but with the electron temperature to the 3/2 power. This is why the dominant wall losses occur in the region of the highest electron temperature.

The power into the anode, from Eq. (7.3-47), can be written as

$$P_a = 2I_d T_{\mathrm{eV}}(\text{anode}). \qquad (7.3\text{-}53)$$

where the electron temperature in this case is evaluated near the anode. The power radiated is

$$P_R = n_o n_e \langle \sigma_* \nu_e \rangle V, \qquad (7.3\text{-}54)$$

where the excitation reaction rate coefficient is given in Appendix E as a function of the electron temperature, and V is the volume of the high-temperature plasma region in the channel, which can be taken to be the channel cross-sectional area times the axial thickness L. Equations (7.3-52) and (7.3-54) require knowledge of the plasma density in the high-temperature region in the channel. This can be found to first order from the beam current

$$n_e = \frac{I_b}{e\nu_b A_c} \approx \frac{\eta_b I_d}{eA_c\sqrt{\dfrac{2\eta_b eV_d}{M}}}, \qquad (7.3\text{-}55)$$

where A_c is the area of the channel exit. Finally, the power to produce the ions in the thruster is the sum of the beam current and the ion current to the walls times the ionization potential:

$$P_{\mathrm{ion}} = \left(I_b + I_{iw}\right)U^+ = \left[\eta_b + I_{ew}\left(1-\gamma\right)\right]I_d U^+, \qquad (7.3\text{-}56)$$

where I_{iw} is given by Eq. (7.3-28) and I_{ew} is given by the left-hand side of Eq. (7.3-52) divided by $2T_e$ (because the electron energy hitting the wall is already included in this equation).

The peak electron temperature is found by equating the input power to the plasma in Eq. (7.3-51) with the sum of the various loss terms described above, and then iterating to find a solution. For example, the SPT-100 Hall thruster has a channel outside diameter of 10 cm, a channel inside diameter of 7 cm, and runs nominally at a discharge of 300 V at 4.5 A with a current utilization efficiency of 0.7 and a voltage utilization efficiency of 0.95 [6]. From Eq. (7.3-55), the plasma density at the thruster exit is about $1.6 \times 10^{17} \text{m}^{-3}$. The power into the plasma, from Eq. (7.3-51), is about 433 W. Taking the electron temperature at the anode to be 5 eV and the hot-plasma thickness L to be about 1 cm, the power balance equation is satisfied if the electron temperature in the channel plasma is about 25 eV.

It is a common rule-of-thumb in Hall thrusters to find that the electron temperature is about one-tenth the beam voltage [35]. The result in the example above of $T_e \approx 0.08\, V_d$ is consistent with that observation. It is also important to note that nearly 70% of the power deposited into the plasma goes to the dielectric channel walls in the form of electron heating, and that the radiation losses predicted by Eq. (7.3-54) are negligible for this case because the electron temperature is so high. Finally, the ion current to the wall for this example from the solution to Eq. (7.3-28) is 0.52 A, which is about 12% of the discharge current and 8% of the beam current in this thruster. This amount agrees well with the 10% of the ion current going to the wall calculated by Baranov [40] in analyzing Hall thruster channel wear.

7.3.5 Hall Thruster Efficiency (Dielectric Walls)

The efficiency of a Hall thruster with a dielectric wall can be estimated by evaluating the terms in the thruster efficiency given by Eq. (2.5-7), which requires evaluating the total power-loss terms in Eq. (7.3-27) to obtain a value for the effective electrical efficiency. This also illustrates the dominant loss mechanisms in the thruster.

The first term in Eq. (7.3-27), the beam power due to the accelerated ions, P_b, is just $I_b V_b$, where the effective beam voltage will be used. The power loss to the dielectric wall will be estimated for the SPT-100 Hall thruster [4–6] using the analysis of Hobbs and Wesson [39] described in Section 7.3.3. The heat flux to the wall was given by Eq. (7.3-46):

$$P_w = I_{iw}\left[\left(\frac{2M}{\pi m}\right)^{1/2} e^{e\phi_s/kT_e}\left(\frac{kT_e}{e}\right) + \left(\varepsilon - \phi_s\right)\right], \qquad (7.3\text{-}57)$$

where I_{iw} is the ion flux to the wall. Following Hobbs and Wesson, the modification to the Bohm criterion is small and $\mathcal{E} \approx T_e/2$ from the Bohm criterion. From Eq. (7.3-44), the sheath potential for xenon and $BNSiO_2$ walls in the SPT-100 thruster, assuming an average electron temperature along the channel wall of 25 eV, is about –54 V. Plugging these values into Eq. (7.3-57) gives

$$P_w = 45.8 I_{iw} T_{\mathrm{eV}} + 2.65 I_{iw} T_{\mathrm{eV}} = 48.5 I_{iw} T_{\mathrm{eV}}. \qquad (7.3\text{-}58)$$

The first term on the right-hand side is again the electron power loss to the wall (written in terms of the ion current to the dielectric surface), and the second term is the ion power loss. The power loss to the channel wall due to the electron loss term is an order of magnitude larger than the power loss due to ions.

It is convenient in evaluating the efficiency of the thruster to relate the ion current to the wall in Eq. (7.3-58) to the beam current. In the plasma, there is an electric field toward the wall due to the pre-sheath of approximately $T_{\mathrm{eV}}/2r = T_e/w$. There is also the axial electric field of V_b/L producing the beam energy. It is common in Hall thrusters to find that the electron temperature is about one-tenth the beam voltage [35], and the channel width is usually approximately L [4,20]. Therefore, the axial electric field is on the order of 10 times the radial electric field. On average, then, the ion current to the channel walls will be about 10% of the beam current. This very simple argument agrees with the SPT-100 example results given in the previous section and the results of Baranov [40].

Using Eq. (7.3-58) with the above estimates for the ion current and electron temperature, the power loss to the insulator walls is

$$P_w = 48.5 I_{iw} T_{\mathrm{eV}} = 48.5(0.1 I_b)(0.1 V_b) = 0.49 I_b V_b. \qquad (7.3\text{-}59)$$

The power loss to the anode is due to the plasma electrons overcoming the sheath potential at the anode surface. From Eq. (7.2-24), the anode electron current is

$$I_{ea} = I_d + I_{ia}. \qquad (7.3\text{-}60)$$

Neglecting the ion current to the anode as small (due to the mass ratio), and realizing that each electron deposits $2kT_e/e$ to the anode for positive plasma potentials (from Appendix C), the power to the anode is

$$P_a = 2T_{\mathrm{eV}} I_d \,. \tag{7.3-61}$$

The electron temperature near the anode is very low, typically less than 5 eV [34–36]. Using the thruster current utilization efficiency and assuming $\eta_b = 0.7$ and $T_{\mathrm{eV}} = 0.01V_b$ near the anode, this can be written as

$$P_a = 2\eta_b I_b (0.01V_b) = 0.014 I_b V_b \,. \tag{7.3-62}$$

The power required to produce the ions is given by Eq. (7.3-56). This can be written as

$$P_{\mathrm{ion}} = \left(I_b + I_{iw}\right) U^+ = \left(1 + \eta_b\right) I_d U^+ \,. \tag{7.3-63}$$

Taking the beam utilization efficiency as 0.7 and estimating that the ionization potential is roughly 5% of the beam voltage, the power required to produce the ions is approximately $P_i = 0.09\ I_d V_b$. The radiation power and other power loss mechanisms are small and will be neglected in this simple example.

The total discharge power into the thruster is then

$$P_d = I_b V_b + 0.49\ I_b V_b + 0.014\ I_b V_b + 0.09\ I_b V_b = 1.59\ I_b V_b \,. \tag{7.3-64}$$

The electrical efficiency of the dielectric-wall thruster is then

$$\eta_e = I_b V_b / (1.59\ I_b V_b) = 0.63 \,. \tag{7.3-65}$$

The total thruster efficiency, assuming the same beam divergence and double-ion content as evaluated above and a mass utilization efficiency of 95% reported for SPT thrusters [4], is

$$\eta_T = (0.915)^2\ (0.63)(0.95) = 50\% \,. \tag{7.3-66}$$

The SPT-100 thruster is reported to run at about 50% efficiency. Since the power loss is dominated by the electron wall losses, this analysis illustrates how critical the wall material selection is to minimizing the secondary electron yield and maintaining a sufficient wall sheath potential for good efficiency. For example, if the wall had been made of alumina and the electron temperature was about 20 V, the sheath potential would be $-1.02T_{\mathrm{eV}}$ in the space charge–limited regime. The wall power from Eq. (7.3-57) would then be about three times higher than in the $BNSiO_2$ case:

$$P_w = 142 I_{iw} T_{\mathrm{eV}} = 1.4 I_b V_b \,. \tag{7.3-67}$$

The electrical efficiency of the thruster, assuming the same anode loading and energy loss to the beam, would be , $\eta_e \approx 0.40$ and the total efficiency would be

$$\eta_T = (0.915)^2\,(0.40)(0.95) \approx 32\%. \qquad (7.3\text{-}68)$$

Recent parametric experiments in which different wall materials were used in the SPT-100 [33] showed that changing from $BNSiO_2$ to alumina reduced the efficiency to the order of 30%, consistent with the increased secondary electron yield of the different wall material.

The agreement of this simple analysis with the experimentally measured efficiencies is somewhat fortuitous because the predictions are very sensitive to the secondary electron yield of the wall material and the actual sheath potential. Small errors in the yield data, changes in the wall material properties during thruster operation, and inaccuracies in the empirical values for the electron temperature and ion flux with respect to the beam parameters will significantly affect the calculated results. Other effects may also be significant in determining the thruster efficiency. The analysis of the sheath potential assumed a Maxwellian electron distribution function. It was recognized several years ago [37,41,42] that the electron distribution may not be Maxwellian. Detailed kinetic modeling of the Hall thruster channel plasma [43,44] indicates that the electron velocity distribution is depleted of the high-energy tail electrons that rapidly leave the plasma along the magnetic field lines and impact the wall. This is especially true near the space-charge limit where the sheath voltage is small and a large fraction of the electron tail can be lost. The collision frequencies and thermalization rates in the plasma may be insufficient to re-populate the Maxwellian tail. This will effectively result in a lower electron temperature in the direction parallel to the magnetic field toward the walls [45], which can increase the magnitude of the sheath potential and reduce the electron heat loss to the wall. In addition, re-collection of the secondary electrons at the opposite wall [46,47], due to incomplete thermalization of the emitted secondary electrons in the plasma, modifies the space-charge limits and sheath potential, which also can change the electron heat flux to the wall.

These effects are difficult to model accurately due to the presence of several different electron populations, several collision/thermalization processes, the effect of magnetization on the electrons, and the presence of plasma instabilities. Understanding what determines the electron temperature and velocity distribution as a function of the discharge voltage and current, and uncovering the effects that determine the wall power flux and finding techniques to minimize them, are continuing areas of research at this time.

7.3.6 TAL Hall Thruster Efficiency (Metallic Walls)

As with the 1.35-kW SPT-100 Hall thruster example above, an estimate will be made of the power loss terms in Eq. (7.3-27) to obtain an electrical efficiency for the 1.4-kW D-55 TAL thruster [29]. Equation (2.5-7) will then be used to obtain an estimate for the thruster efficiency. The beam power P_b is, again, just $I_b V_b$. As stated in the previous section, the wall losses (P_w) are essentially negligible in TAL thrusters, and the power to the anode is given by Eq. (7.3-49):

$$P_a = 2T_{\mathrm{eV}} \frac{I_b}{\eta_b} = 0.29 I_b V_b \,. \tag{7.3-69}$$

In Eq. (7.3-69), it is again assumed $\eta_b = 0.7$ and $T_{\mathrm{eV}} = 0.1 V_b$, although these values may be somewhat different in TAL thrusters. The power to produce the ions is again approximately $0.09 I_b V_b$.

The total discharge power, Eq. (7.3-27), then becomes

$$P_d = I_b V_b + 0.29\, I_b V_b + 0.09\, I_b V_b = 1.4\, I_b V_b \,. \tag{7.3-70}$$

Neglecting the power in the cathode keeper (if any) and the magnet as small compared to the beam power, the electrical utilization efficiency from Eq. (2.5-1) is then

$$\eta_e = \frac{P_d}{1.4 P_d} = 0.72 \,. \tag{7.3-71}$$

The total thruster efficiency, assuming a 10% double-ion content, a 20-deg angular divergence [29,48], and a 90% mass utilization efficiency reported for TAL thrusters [29,49], is then, from Eq. (2.4-7),

$$\eta_T = (0.915)^2\, (0.72)(0.9) = 54\% \,. \tag{7.3-72}$$

This result is on the same order as that reported in the literature [29,49,50] for this power-level TAL and is essentially the same as the SPT-100 efficiency in this simple example if the wall losses had been included. However, the power loss to the anode is seen as the dominant mechanism in the TAL efficiency.

7.3.7 Dielectric-Wall Versus Metallic-Wall Comparison

It is interesting to make a few direct comparisons of dielectric-wall Hall thrusters with metallic-wall TAL thrusters. Similar discussions have appeared in the literature [1,3,31], often with conflicting opinions. The basic plasma physics in the channel described above applies to both the dielectric-wall Hall thruster and the TAL. The maximum electron temperature occurs in both thrusters near the channel exit in the region of strongest magnetic field where the Hall current is a maximum. The different interaction of the thruster walls with this plasma determines many of the characteristics of the thruster, including life. Dielectric-wall thrusters have a significant amount of their input power deposited as loss on the dielectric channel walls due to electron bombardment. In the above example efficiency calculation, approximately 25% of the power going into the thruster was deposited on the channel walls. The metallic walls in TAL thrusters collect a smaller electron current because they are biased to cathode potential, and they also tend to have a small exposed area in poor contact with the plasma, which limits the amount of ion and power lost to these surfaces. However, the anode is positioned very close to the high electron temperature region and receives a significant amount of power deposition in collecting the discharge current. In the above example TAL efficiency calculation, over 20% of the power going into the thruster was deposited on the anode.

The deep channel in dielectric-wall Hall thrusters, with a low magnetic field strength and low electron temperature near the anode, tends to minimize the power deposition on the anode. In the above simple example, only 1% of the thruster input power was deposited on the anode. Nevertheless, the anode is normally electrically isolated from the thruster body (and therefore thermally isolated), and so anode overheating is sometimes an issue, especially at high power density. The anode in TAL thrusters can also have heating issues because the loading is much higher, even though the view factor for the anode to radiate its power out of the thruster is better than the deep channel in the insulting-wall configuration. In addition, with the anode positioned physically close to the thruster exit in TALs, impurity deposition and material buildup problems can occur. This has been an issue in ground testing of some TAL thrusters [29], where carbon deposition on the anode from back sputtering from the beam dump became significant over time. TAL thrusters with deeper channels can be designed and operated [3]. The performance of the thruster is likely different in this configuration, and ion bombardment and sputtering of the metallic channel walls can become significant and affect the thruster life.

Dielectric-wall Hall thrusters are often described in terms of an ionization zone upstream of the exit plane and an acceleration zone in the region of the exit plane. TAL thrusters have a similar ionization region near the magnetic field maximum, which is now closer to the anode because the magnetic field gradient is greater. The TAL acceleration zone is described as being a layer close to the anode [1,3] that can extend outside of the thruster [48]. The higher electron temperatures associated with TAL thrusters support higher electric fields in the quasi-neutral plasma, which compresses these zones relative to dielectric-wall thrusters. In addition, the metallic walls and higher electric fields are conducive to multiple acceleration stages, which can improve thruster performance and produce higher Isp than a conventional single-stage TAL thruster [1,51]. Multiple-stage dielectric-wall Hall thrusters that operate at high Isp have also been investigated (see [17] and the references cited therein).

Finally, the difference between dielectric-wall Hall thrusters and TAL thrusters is sometimes attributed to the secondary electron coefficients of the different wall materials. The above discussion shows that this is not the dominant difference. Instead, the proximity of the TAL anode electrode to the high temperature plasma region and the thruster exit plane is what changes the electric field profile, power deposition, and sputtering characteristics as compared to the dielectric-wall Hall thruster.

7.4 Channel Physics and Numerical Modeling

As discussed in the previous sections, the detailed physics determining Hall thruster performance is not well understood. Specifically, the electron distribution function in the exit region, the mechanisms responsible for electron transport across the magnetic field, and the role of oscillations on the particle transport and plasma conditions need to be determined. A considerable effort has been made to develop fluid, kinetic, hybrid, and particle-in-cell (PIC) models to predict and explain the performance and effects observed in Hall thrusters. Hirakawa and Arakawa developed [52] a two-dimensional (2-D) particle-in-cell model where anomalous electron diffusion was introduced by using oscillating azimuthal electric fields. Boeuf and Garrigues developed a one-dimensional (1-D) hybrid model [53] in which the electrons were treated as a fluid and the ions were described by a collisionless Vlasov (kinetic) equation. Similar fluid and hybrid models have been developed by other authors [54–56] using various techniques to determine the ion transport, such as Monte-Carlo simulation, Boltzman equation solutions, and “ion free-fall” (essentially a Bohm current solution) to the boundaries. The most widely used code, HPHall, is a 2-D, transient hybrid model originated by Fife and Martinez-Sanchez [30] that has been recently extended with an improved sheath model [41,42,57] and a model of channel erosion [58,59].

7.4.1 Hybrid Hall Thruster Models

Hybrid Hall thruster models, such as HPHall [30, 57], utilize a steady-state fluid electron momentum equation and a time-dependent electron energy equation to solve for electron temperature and potentials in the channel and plume. The codes also use time-dependent ion and neutral particle equations to calculate the plasma density and ion velocities on a time scale much larger than the electron time scale. These codes are also used to model Hall thruster transit-time oscillations that are on the order of time scales related to neutral atom and ion motions (≤1 MHz) but cannot capture the effects of electron instabilities that have much higher frequencies.

From the steady-state electron momentum equation, an Ohm's law representation from Eq. (3.6-20) for the electron field is

$$\eta \mathbf{J}_e = \mathbf{E} + \frac{\nabla \mathbf{p} - \mathbf{J}_e \times \mathbf{B}}{en} - \eta_{ei} \mathbf{J}_i , \tag{7.4-1}$$

where the resistive term has the following form in the magnetic frame of reference:

$$\eta \mathbf{J} = \eta_{\perp} J_{\perp} + \eta_{\parallel} J_{\parallel} + \eta_{\wedge} J_{\wedge} , \tag{7.4-2}$$

and the subscripts represent the directions perpendicular, parallel, and transverse (in the $\mathbf{E} \times \mathbf{B}$ direction), respectively, to the local magnetic field.

Equation 7.4-1 must be separated into the two components of the $\mathbf{J}_e \times \mathbf{B}$ motion in a manner similar to that in Section 3.6 and solved for the electric field. From current conservation, the electron current is taken to be the difference between the discharge current and the ion current from the particle calculations. Typically, the circuit current is chosen at each time step to satisfy the applied voltage ($= \int \mathbf{E} \cdot \mathbf{d}\ell$) boundary conditions.

7.4.1.1 Transverse Electron Transport. Writing the perpendicular resistivity in terms of the perpendicular electron mobility, as defined in Eq. (3.6-66), gives

$$\eta_{\perp} = \frac{1}{en\mu_{e\perp}} = \frac{1 + \omega_c^2 \tau_m^2}{en\mu_e} = \frac{1 + \omega_c^2 / \nu_m^2}{en\mu_e} , \tag{7.4-3}$$

where the collision time τ_m for momentum transfer is equal to one over the collision frequency ($1/\nu_m$). The perpendicular electron flux from Ohm's law, Eq. (7.4-1), can then be written as

$$J_{e\perp} = \mu_{e\perp}\left(enE_{\perp} + \frac{\partial p_e}{\partial x}\right) - \frac{\mu_{e\perp}}{\mu_{ei}} J_{i\perp}, \tag{7.4-4}$$

and the electron mobility due only to electron–ion collisions is given by

$$\mu_{ei} = \frac{e}{m\nu_{ei}}. \tag{7.4-5}$$

Usually, the ion flux term in Eq. (7.4-4) is neglected and an effective electric field is used such that the electron flux is expressed as

$$J_{e\perp} = en\mu_{e\perp}E'_{\perp}, \tag{7.4-6}$$

where the effective electric field is

$$E'_{\perp} = \left(E_{\perp} + \frac{1}{en}\frac{\partial p_e}{\partial x}\right). \tag{7.4-7}$$

The effective perpendicular electron mobility in Eq. (7.4-4) is

$$\mu_{e\perp} = \frac{e}{m\nu_m}\frac{1}{1+\omega_c^2/\nu_m^2} = \frac{\mu_e}{1+\Omega_e^2}, \tag{7.4-8}$$

where Ω_e^2 is the electron Hall parameter, and the momentum-transferring collision frequency ν_m is described, as in Chapter 3, by

$$\nu_m = \nu_{ei} + \nu_{en}. \tag{7.4-9}$$

This expression for the transverse electron mobility then accounts for both electron–ion and electron–neutral collisions in the partially ionized plasma.

Since the electrons are well magnetized in the plasma near the exit of the channel where the magnetic field strength is the highest, the electron Hall parameter is much greater than unity and the transverse electron mobility across the field lines is found to be small. In fact, calculations of the electron collision frequency based on the classical collision terms in Eq. (7.4-9) are unable to provide sufficient cross-field transport to support the discharge current passing through the thruster [54,57,59]. In addition, the neutral density in the plume of the Hall thruster is low due to the high mass utilization efficiency, which reduces the effective collision frequency in Eq. (7.4-9) and again leads to problems in providing sufficient transport of the electrons from the external

cathode across the transverse field lines and into the channel to support the discharge current. Two mechanisms have been proposed in an attempt to describe "enhanced" cross-field electron transport and explain the observed Hall thruster operation.

Morozov [12] postulated that electron-wall interactions in the channel region will scatter electron momentum and introduce secondary electrons, which can increase the effective cross-field transport. This effect is introduced into the effective collision frequency by a wall-scattering frequency ν_w:

$$\nu_m = \nu_{ei} + \nu_{en} + \nu_w . \tag{7.4-10}$$

The wall-scattering frequency is either given by $\alpha * 10^7$ per second [53], with α an adjustable parameter used to match the experimental data, or the wall collision frequency of electrons is calculated directly in the code [59]. While this effect does increase the electron transport in the channel, it is sometimes found to provide insufficient enhancement of the electron transport. In addition, in the plume of the thruster there are no walls and the neutral density is very low, which precludes the use of Eq. (7.4-10) to increase the cross-field transport sufficiently to explain the experimental data.

Additional cross-field transport has been added in the codes by invoking Bohm diffusion both inside and outside the thruster channel. As discussed in Chapter 3, Bohm diffusion likely arises from $\mathbf{E} \times \mathbf{B}$ driven drift instabilities, which can naturally occur in these thrusters due to the Hall current. Using the Bohm diffusion coefficient from Eq. (3.6-72) and the Einstein relationship of Eq. (3.6-28), a Bohm mobility can be defined as

$$\mu_B = \frac{1}{\beta B} = \frac{e}{\beta m \omega_c}, \tag{7-4-11}$$

where β is an adjustable coefficient changed to make the code predictions of the thruster parameters fit the experimental data. If full Bohm diffusion is required by the code to match the data, such as is often the case in the plume, then β = 16. The effective Bohm collision frequency is then

$$\nu_B = \beta \omega_c . \tag{7-4-12}$$

The total "anomalous" collision frequency used in the codes is

$$\nu_m = \nu_{ei} + \nu_{en} + \nu_w + \nu_B , \tag{7.4-13}$$

where the wall collision frequency ν_w is neglected in the plume.

7.4.1.2 Transport Along the Magnetic Field. In the direction along the magnetic field lines, the $\mathbf{J}\times\mathbf{B}$ cross product in the electron momentum equation is zero and Eq. (7.4-1) becomes

$$\eta J_e = E + \frac{\nabla p}{en} - \eta_{ei} J_i \,. \tag{7.4-14}$$

The electric field along the field line is then

$$E = \frac{\nabla p}{en} + \eta J_e - \eta_{ei} J_i = -\nabla\phi \,. \tag{7.4-15}$$

With the standard assumptions used along magnetic fields in many plasmas of zero net current ($j_e \approx j_i$) and uniform electron temperature, Eq. (7.4-15) can be solved for the potential along the field line to give

$$\phi = \phi_o + T_e \ln\left(\frac{n}{n_o}\right). \tag{7.4-16}$$

This equation was derived in Section 3.5-1 and represents the simple Boltzman relationship for plasmas with Maxwellian electron distribution functions. It is often called the *barometric law* in ion thruster literature and the *thermalized potential* in Hall thruster literature. Thus, the transport along the magnetic field lines is usually considered to be classical.

It is commonly assumed that the density gradient along the magnetic field line is relatively small, so the potential change along a magnetic field line from Eq. (7.4-16) is essentially zero. Therefore, within about kT_e/e, the magnetic field lines represent equipotential lines in the plasma. The simplifying assumptions leading to this conclusion (zero net current, Maxwellian electrons, and small density gradient along the magnetic field lines) are often used and may introduce significant errors in some cases. Nevertheless, the thermalized potential has been used for many years [3] in the design of Hall thrusters to relate the magnetic field shape to the electric field in the plasma [11].

7.4.1.3 Continuity and Energy. Continuity for the neutrals in the thruster can be expressed as

$$\frac{\partial n_o}{\partial t} + v_o \nabla n_o = -n_e n_o \langle \sigma_i v_e \rangle, \tag{7.4-17}$$

where the right-hand side represents the local ionization rate. For ions and electrons, continuity in the plasma gives

$$\nabla \cdot \mathbf{J}_e = \nabla \cdot \mathbf{J}_i . \tag{7.4-18}$$

In addition, charge balance at the insulating wall dictates that

$$J_i = J_e - J_{se}, \tag{7.4-19}$$

where J_{se} is the secondary electron current density, which is equal to the secondary electron yield γ times the incident electron flux.

The electric field in the perpendicular direction ($\hat{z}$) in the plasma can be found from Eq. (7.4-4):

$$E = \frac{J_e}{en_e\mu_{e\perp}} - \frac{1}{en_e}\frac{\partial\left(n_e kT\right)}{\partial z} + \frac{\mu_{e\perp}}{\mu_{ei}} J_i . \tag{7.4-20}$$

The potential applied across the plasma is then

$$V = -\int_0^L E(z,t)dx , \tag{7.4-21}$$

which can be used to find the electron current or total current flowing in the plasma.

The electron energy equation is

$$\frac{\partial}{\partial t}\left(\frac{3}{2} n_e \frac{kT_e}{e}\right) + \nabla \cdot \frac{5}{2} T_e \mathbf{J}_e = \mathbf{E} \cdot \mathbf{J}_e - R - S - P_w, \tag{7.4-22}$$

where $\mathbf{E} \cdot \mathbf{J}_e$ is the ohmic power input, R is the radiative energy loss, S is the ionization energy loss, and P_w is the electron energy loss to the walls. The radiative energy loss is

$$R = U^* n_e n_o \left\langle \sigma_* v_e \right\rangle , \tag{7.4-23}$$

and the ionization energy loss is given by

$$S = U^+ n_e n_o \left\langle \sigma_i v_e \right\rangle . \tag{7.4-24}$$

The ionization and excitation reaction rate coefficients in Eqs. (7.4-23) and (7.4-24) are given in Appendix E. Finally, the electron energy density is given by convection in the plasma as

$$\varepsilon = \frac{5}{2} n_e k T_e. \tag{7.4-25}$$

7.4.1.4 Ion Current. Several methods have been used to describe the ion generation and transport in the Hall thruster models. First, the ions have been modeled as a fluid using continuity equations [54,60], where the axial motion is due to the electric field along the channel and the radial motion to the wall is determined by the ion-neutral scattering frequency. The ion current to the wall is then

$$I_w = n_i n_o \langle \sigma_{\text{in}} v_i \rangle A_w L\,, \tag{7.4-26}$$

where A_w is the wall area, L is the plasma length, σ_{in} is the ion-neutral collision cross section for 90-deg scattering including elastic and charge-exchange collisions, and the velocity of the neutrals is neglected relative to the ion velocity. In PIC numerical codes, this represents the radial flux to the cell boundary where $A_w L$ becomes the cell volume.

Fife [30] modeled the ion motion using a 2-D PIC code that assumed the ions and neutrals acted as discrete macro-particles in each cell. The time step in the ion-PIC code, in this case, was adjusted (to typically three orders of magnitude slower than the electron model time step) to handle the ion-motion time scales without invoking excessive computational time.

Finally, the ion Vlasov equation has been used to solve for the ion generation and motion [52,53]. This has primarily been applied for investigating low-frequency oscillations on the order of the ion-characteristic time scales. In one dimension, this can be written as

$$\frac{\partial f}{\partial t} + v_x \frac{\partial f}{\partial t} + \frac{e}{M} E \frac{\partial f}{\partial v_x} = n_e n_o \langle \sigma_i v_e \rangle \delta(v_x - v_o), \tag{7.4-27}$$

where f is the ion distribution function and $\delta(v_x - v_o)$ is the Dirac delta function evaluated for the ion velocity relative to the neutral velocity. The ion density is then found from

$$n_i = \int f(x, v_x, t) dv_x\,. \tag{7.4-28}$$

The plasma is always assumed to be quasi-neutral ($n_i \approx n_e$). At the sheath boundary at the wall, the ion current normally is assumed to be the Bohm current and the electron current is the one-sided random electron flux. Total current continuity requires the ion flux and net electron flux (incident electrons and emitted secondary electrons) to the insulating walls to be equal, which establishes the sheath potential to produce quasineutrality and charge conservation as described above. The hybrid-model equations described above for determining the ion currents are normally evaluated numerically in either 1-D or 2-D with greatly different time steps between the electron fluid evolution and the ion and neutral motion evaluations.

7.4.2 Steady-State Modeling Results

The physics of the Hall thruster discharge related to the transverse electron mobility, electron-wall interactions, and the exact nature of the electron distribution function are not completely understood at this time. However, the 1-D and 2-D models described above are reasonably successful in predicting plasma parameters and thruster behavior provided enhanced electron conductivity is incorporated in the channel due to wall collisions and turbulence, and modifications to the wall heat fluxes are made associated with the secondary electron behavior. In addition, enhanced electron transport in the plume region near the thruster exit is required to match the models' predictions with the experimental results [61], which is normally provided by assuming collective oscillations drive Bohm-like diffusion. In this region, other mechanisms may also be responsible for the cross-field electron transport, and research in this area to determine the responsible mechanism(s) is continuing.

The hybrid codes can provide very reasonable predictions of the steady-state plasma parameters in the thrusters. For example, Fig. 7-14 shows the average profiles (along the channel axis) predicted by a 1-D model [53] for the potential, electric field, plasma density, mean electron energy, neutral density, and ionization rate for the SPT-100 Hall thruster, where 4 cm corresponds to the channel exit. The average plasma density peaks upstream of the exit, as is also predicted by the 2-D HPHall code [30] result shown in Fig. 7-15 for the SPT-100 Hall thruster channel. In both cases, there is a characteristic peak in the plasma density upstream of the channel exit in the ionization region, and a decreasing plasma density is seen moving out of the channel as the ions are accelerated in the electric field of the acceleration region. The plasma density prediction by the 1-D code is slightly lower than the 2-D HPHall result because of differences in the heat flux calculation to the wall and the resulting values of

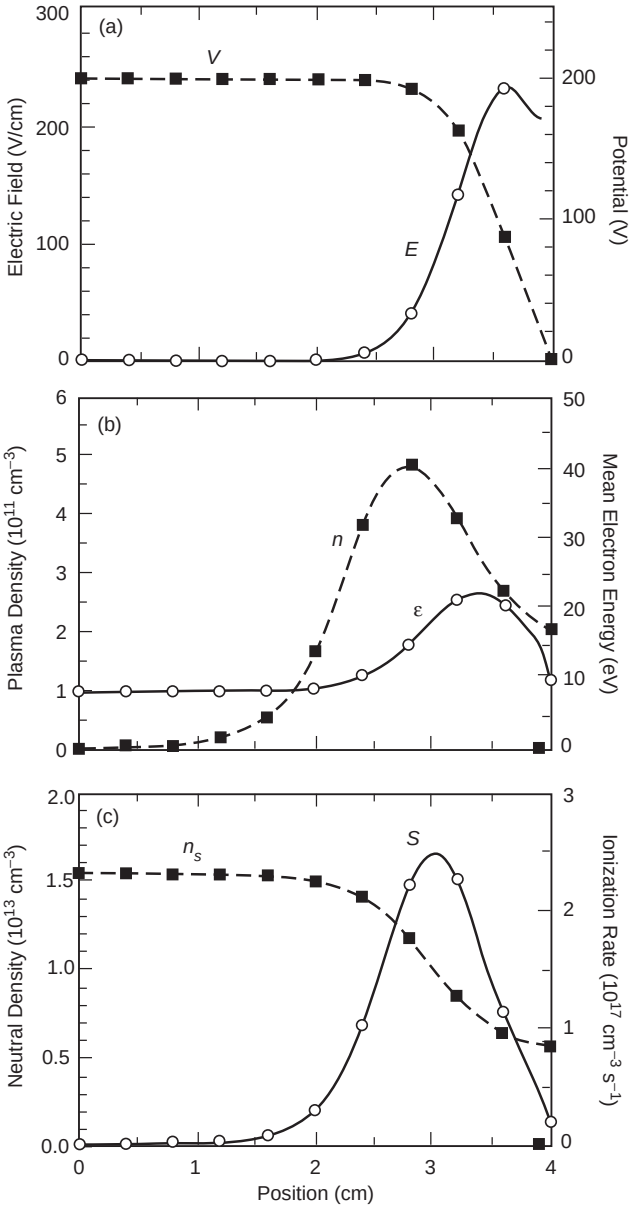

Fig. 7-14. 1-D Hall thruster code [53] for the SPT-100: (a) potential and electric field, (b) plasma density and electron energy, and (c) neutral density and ionization rate (redrawn from [53]).

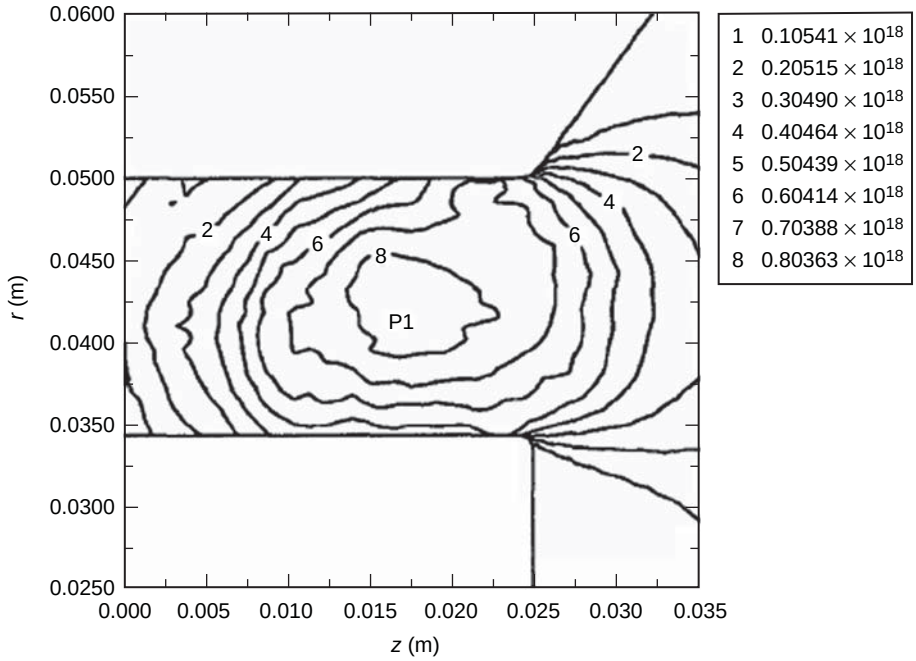

Fig. 7-15. Average plasma density computed by HPHall for the SPT-100, with the peak plasma density at P1 = 8×10^{17} m^{-3} (from [30]).

the electron temperature. Since the distribution function of the electrons can certainly be non-Maxwellian and anisotropic, the actual value of the density in the Hall thruster will differ somewhat from the values calculated by these existing codes.

The profiles shown by the 1-D code results in Fig. 7-14 suggest that three overlapping but distinct regions exist in the plasma channel of a well-designed Hall thruster. Near the anode, the potential drop is small due to the low magnetic field in this region, resulting in good plasma conduction to the anode but small ionization. The ionization zone occurs upstream of the channel exit where the neutral gas density is still high and the electrons are well confined and have significant temperature. The acceleration zone exists near the channel exit where the electric field is a maximum, which occurs at this location because the magnetic field is a maximum and the transverse electron mobility is significantly reduced as described above. Outside the channel, the electric field, plasma density, and electron temperature drop as the magnetic field strength decays and the Hall current decreases.

The current versus voltage predictions from the 1-D code [53] for different values of the transverse magnetic field in the channel for the SPT-100 thruster are shown in Fig. 7-16. As the transverse magnetic field increases, the impedance of the discharge increases significantly and higher voltages are required to obtain the transverse electron mobility required to achieve the desired discharge current. Increases in the mass flow rate increase the collisional effects in the plasma region, and this results in more current at a given voltage and magnetic field. In addition, Fig. 7-16 shows regions where the 1-D code predicts oscillatory behavior, as indicted by the solid points. This is discussed in the next section.

The 1-D hybrid code results shown in Fig. 7-16 suggest that the code captures the trend in the discharge impedance as the magnetic field and applied voltage are changed; i.e., the discharge current decreases as the magnetic field increases at a given discharge voltage due to the lower electron mobility. However, the code does not predict the correct current-versus-voltage behavior for this thruster at low voltages. Figure 7-17 shows the current-versus-voltage data for one condition in the SPT-60 (a 60-mm channel outside-diameter version described in [4]). As the discharge voltage is decreased below about 200 V, the current initially increases until the energy of the electrons at very low voltage is insufficient to produce high ionization fractions, and the plasma density and discharge current then fall. Improvements in the electron transport physics are

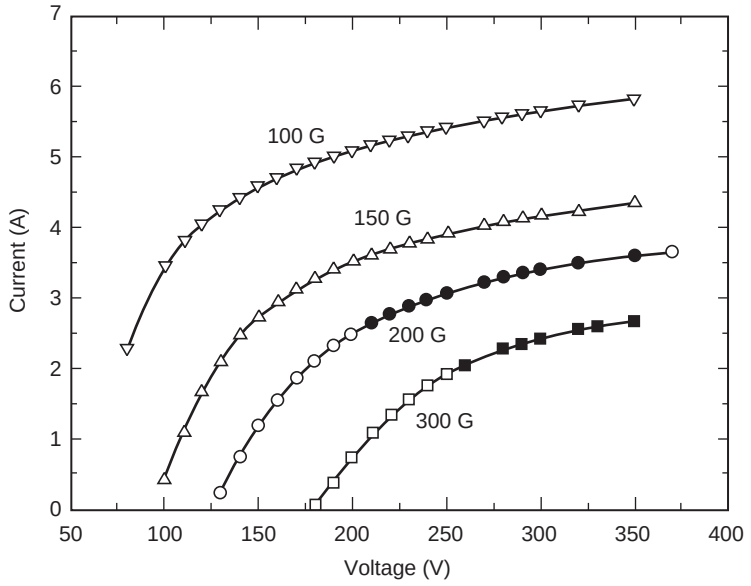

Fig. 7-16. Current-versus-voltage predictions from the 1-D code of Boeuf and Garrigues (from [53]) for the SPT-100, where the solid points indicate regions of predicted oscillations.

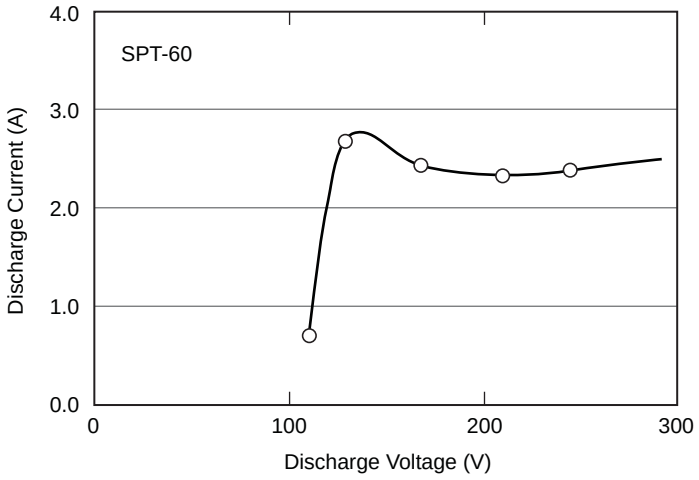

Fig. 7-17. Current versus voltage for one operating condition in the SPT-60 ([redrawn from [4]), showing the non-monotonic current variations usually observed in Hall thrusters at low discharge voltages.

clearly required for the hybrid code to fully predict the Hall thruster behavior. Work continues on developing hybrid codes to better predict the thruster parameters and performance.

7.4.3 Oscillations in Hall Thrusters

Depending on their size and operating characteristics, Hall thrusters have the capability of generating many different waves and instabilities with frequencies from 1 kHz to tens of MHz. A survey of the frequencies of different plasma waves, the characteristic lengths (i.e., of sheaths, etc.) in the thruster, and wave and particle drift velocities expected in typical Hall thrusters was compiled by Choueiri [62]. The most commonly observed oscillations occur in the band of frequencies from 1–30 kHz associated with ionization instabilities and rotational oscillations in the annular discharge channel. Azimuthally propagating waves with frequencies up to 100 kHz that are not associated with ionization instabilities can also occur due to magnetic field gradients [11]. In the range of 100–500 kHz, ion transit time oscillations associated with axial motion of the ions through the ionization and acceleration regions can occur. Above this frequency range, azimuthal drift waves [63] and ion acoustic waves have also been predicted and observed.

The low-frequency time dependence of the ion and neutral behavior can be analyzed with the analytical models [30] by writing the ion conservation equation as

$$\frac{\partial n_i}{\partial t} = n_i n_o \langle \sigma_i v_e \rangle - \frac{n_i v_i}{L}, \tag{7.4-29}$$

and the neutral particle conservation equation as

$$\frac{\partial n_o}{\partial t} = -n_i n_o \langle \sigma_i v_e \rangle + \frac{n_o v_o}{L}, \tag{7.4-30}$$

where v_o is the neutral velocity and L is the axial length of the ionization zone. The perturbed behavior of the ion and neutral densities with time is linearized such that

$$\begin{aligned} n_i &= n_{i,o} + \varepsilon n_i' \\ n_o &= n_{o,o} + \varepsilon n_o', \end{aligned} \tag{7.4-31}$$

where the first term on the right-hand side denotes the unperturbed state. Combining Eqs. (7.4-29), (7.4-30), and (7.4-31) gives

$$\frac{\partial^2 n_i'}{\partial t^2} = n_{i,o} n_{o,o} n_i' \langle \sigma_i v_e \rangle^2 . \tag{7.4-32}$$

This equation represents an undamped harmonic oscillator with a frequency given by

$$f_i = \frac{1}{2\pi} \sqrt{n_{i,o} n_{o,o} \langle \sigma_i v_e \rangle^2} \approx \frac{v_i v_o}{2\pi L}. \tag{7.4-33}$$

The low-frequency oscillatory behavior of Hall thrusters is related to the velocities of the ions and neutrals relative to the scale length of the ionization zone. This indicates that periodic depletion of the neutral gas in the ionization region causes the ion density to oscillate, which impacts the electron conductivity through the transverse magnetic field and thereby the discharge current. The ionization region location can then oscillate axially in the channel on the time scale of neutral replenishment time. The models show [53] that the oscillation depends strongly on the magnetic field strength near the channel exit, and that optimum operation of the thruster generally corresponds to high mass utilization regimes where this instability occurs.

These types of oscillations, which are typically observed in the discharge current when the thrusters are operated in a voltage-regulated mode, have been called “breathing modes” [53] and “predator–prey modes” [30], and an example is shown in Fig. 7-18 for the SPT-100 Hall thruster [55]. The frequency in this experimentally observed example is about 17 kHz. However, the frequency depends on the thruster operating conditions and can range from 10 to 30 kHz for different flow rates, voltages, and magnetic fields. The 1-D numerical code

[53] predictions for the total current, electron current, and ion current at the thruster exit for the SPT-100 are shown in Fig. 7-19. In this case, a frequency of 16 kHz is predicted, in good agreement with the experimental data.

Similar predictions about the low-frequency oscillation behavior of Hall thrusters from the 2-D HPHall code are shown in Fig. 7-20, where the anode current and beam current are plotted versus time. The predicted frequency in this case is 11 kHz, which is less than the value shown in the example of Fig. 7-18. This is likely due to an under-prediction of the electron temperature in the ionization region of the channel [30] by this version of the code.

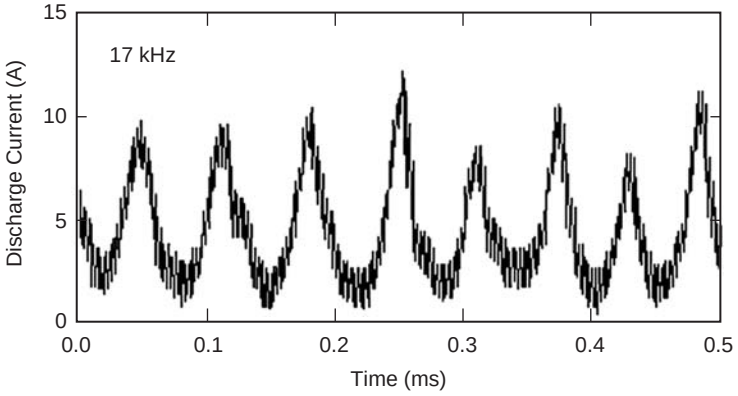

Fig. 7-18. Measured evolution of the discharge current for the SPT-100 (from [55]).

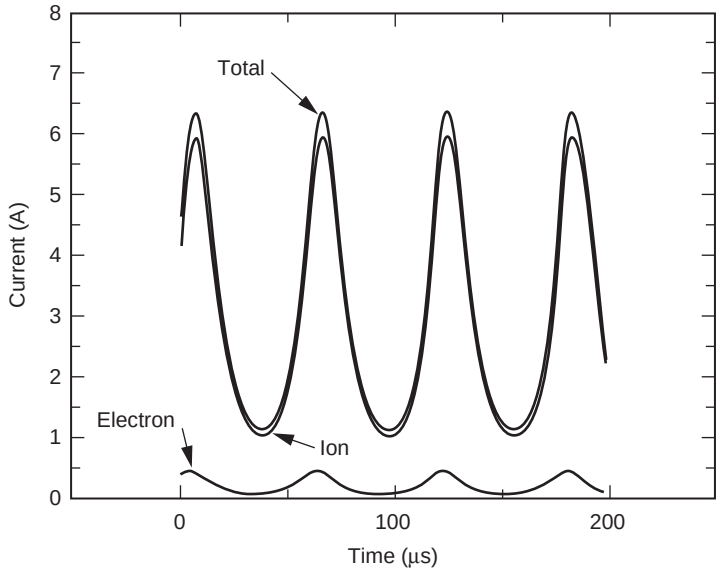

Fig. 7-19. Oscillating current predictions from the 1-D code for the SPT-100 (from [53]).

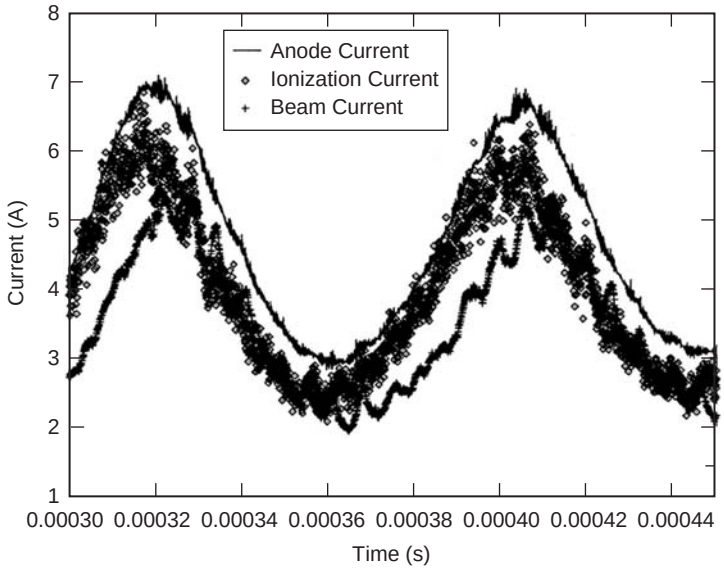

Fig. 7-20. Anode current, ionization, and beam current calculated by HPHall for the SPT-70 Hall thruster (from [30]).

However, the ionization instability driving these oscillations is the same as that analyzed in the 1-D model, and so the behavior of the instability is adequately reproduced by the 2-D model. The low-frequency oscillations can reach 100% of the discharge current depending on the voltage and mass flow (current) for a given thruster design. However, more modern designs, especially those intended for flight, typically have much lower oscillation amplitudes.

7.5 Hall Thruster Life

The operating time and total impulse of a Hall thruster is determined primarily by erosion of the channel wall and the life of the cathode. Hollow cathode wear-out has not represented a life limitation to date because thruster lifetimes of less than 10,000 hours are typical, and robust LaB_6 hollow cathodes have been used in all of the Russian Hall thrusters. Other issues such as deposited material build-up on the electrodes, conductive-flake production, electrical shorting, etc., are also of concern in evaluating the life of a Hall thruster. However, the erosion of the channel wall by ion bombardment sputtering is a very visible process [4] that changes the channel dimensions and ultimately exposes the magnetic circuit, which, when eroded, can degrade the thruster performance. However, life tests of flight thrusters such as the SPT-100 and the PPS-1350 show that they can take hundreds to thousands of hours for magnetic circuit erosion to significantly alter thruster performance. Of greater concern, in this case, is the sputtering of iron from the magnetic circuit, which would have

a significantly higher impact if deposited on most spacecraft components. Therefore, understanding the wall erosion rate and its dependence on thruster materials and operating parameters is of importance in predicting the thruster life and performance over time and its potential impact on the spacecraft.

The erosion rate, given by the rate of change of the wall thickness, *w*, is

$$\dot{\Re} = \frac{\partial w}{\partial t} = \frac{J_i W}{\rho e A_v} Y(\varepsilon_i), \tag{7.5-1}$$

where J_i is the ion flux, *W* is the atomic weight, ρ is the material density, *e* is the ion charge, A_v is Avogadro's number, and *Y* is the sputtering yield of the material, which is dependent on the ion type and energy ε_i. Since the material properties are known, the issue becomes one of knowing the ion flux, ion energy, and sputtering yield of the wall.

Several analytical models of the Hall thruster have been developed and applied to this problem [37,60,64]. The most accurate predictions have been achieved using a modified 2-D HPHall code [58] to obtain the ion fluxes and energies. The sputtering yield of boron nitride compounds used in dielectric-wall Hall thrusters has been measured by Garnier [65] versus incidence angle and ion energy, and is used in several of these models. However, the Garnier data are at only a few energies and in excess of 300 V. Gamero extrapolated these data to lower energies using the semi-emperical sputtering law scaling of Yamamura and Tawara [66], obtaining the following expression for the sputtering yield in units of mm^3/coulomb:

$$Y = \left(0.0099 + \alpha^2 6.04\times10^{-6} - \alpha^3 4.75\times10^{-8}\right)\sqrt{\varepsilon_i}\left(1-\sqrt{\frac{58.6}{\varepsilon_i}}\right)^{2.5}, \tag{7.5-2}$$

where α is the incident angle of the ion. In Eq. (7.5-2), the value 58.6 represents the estimated threshold energy for sputtering required by Yamamura's model. Figure 7-21 shows an example of the yield predicted by Eq. (7.5-2) for two different incidence angles. Equation (7.5-2) was shown [58] to accurately fit the data of Garnier and provides projections of the sputtering yield down to low ion energies predicted by HPHall deeper in the channel.

Figure 7-22 shows the predicted [58] and experimentally measured erosion profiles [67] for the SPT-100 thruster inner and outer channel walls. Good agreement with the observed channel erosion is seen near the thruster exit, and the profiles have the correct functional shape. It is likely that inaccuracies in the extrapolated sputtering yield at low energies caused the disagreement with the

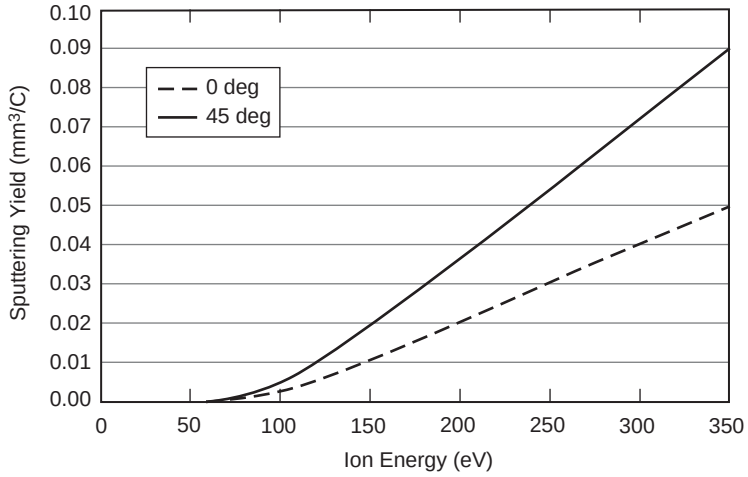

Fig. 7-21. Sputtering yield calculated for singly ionized xenon on $BNSiO_2$ versus ion energy for two incidence angles.

data deep in the channel. This can be remedied by additional sputter-yield measurements at low energy and a refinement of the sputtering yield in Eq. (7.5-2).

It is possible to develop some simple scaling rules for Hall thruster erosion in the magnetized plasma region near the exit plane. It was estimated in Section 7.3.4 that the ion flux to the wall in dielectric-wall Hall thrusters was about 10% of the beam current. It can be assumed that the energy of the ion flux to the wall is related to the beam energy, which is proportional to the discharge voltage. An examination of Fig. 7-21 shows that the sputtering yield is essentially a linear function of the ion energy. The erosion rate in Eq. (7.5-1) then becomes

$$\dot{\Re} \propto K \frac{I_b}{A_w} V_d = K \frac{I_d V_d}{\eta_b A_w}, \tag{7.5-3}$$

where K is a constant, A_w is the wall area, and Eq. (7.3-10) has been used for the beam current efficiency. Equation (7.5-3) shows that the erosion rate of the thruster wall is proportional to the power density in the accelerator channel [4]. This indicates that larger Hall thrusters are required to increase the power for a given operation time as determined by the allowable erosion of the insulator wall thickness. A good rule-of-thumb for the relationship of operation time over a reasonable throttle range of a given Hall thruster design is

power * operation time ≈ constant.

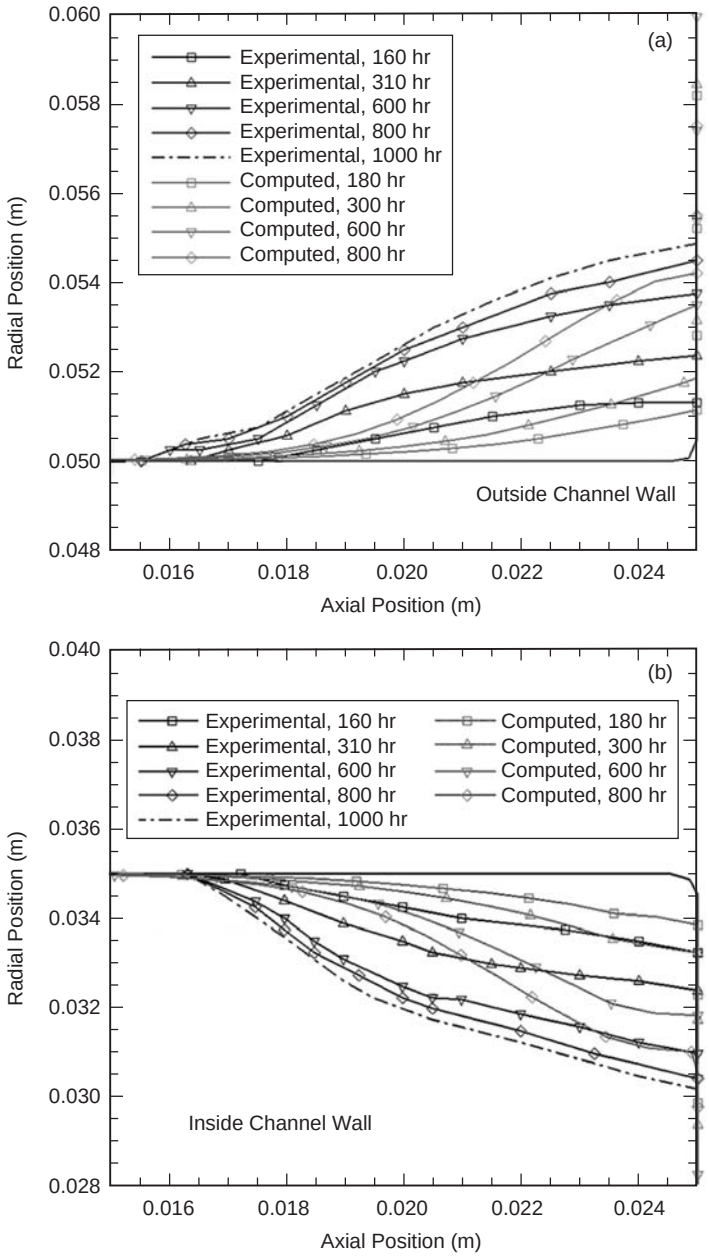

Fig. 7-22. Erosion pattern predicted by the modified HPHall code and measured for the SPT-100 thruster (redrawn from [58]).

Over a limited range, the thrust from a Hall thruster is proportional to the discharge power, and so

$$\text{thrust} * \text{operation time} \approx \text{constant}.$$

This suggests that the total impulse is essentially a constant for a given thruster design. Therefore, operating at lower thrust in throttled mission profiles will result in longer thruster operation time. However, if the throttling is too deep, the thruster performance will degrade (requiring higher input power to produce a given thrust) and the above relationship is no longer valid. Hall thruster throttle ranges of over 10:1 have been demonstrated with good performance, depending on the thruster design.

Finally, the life of TAL thrusters has not been as extensively investigated as the Russian SPT thrusters. The erosion of the channel guard rings has been identified as the primary life-limiting mechanism [29], and alternative materials were suggested to extend the thruster life by reducing the sputtering yield. Since the wall/guard ring is biased at cathode potential, the incident ion energy along the wall depends on the potential profile in the thruster channel and past the exit plane. This certainly influenced the selection of the TAL anode placement and the design of the anode/channel region to minimize the ion energy (and flux) to the walls. The dielectric-wall Hall thrusters limited the ion energy to the floating potential ($\approx 6T_e$ for xenon) for wall materials with very low secondary electron yield, and to lower energies with materials that have secondary electron yields approaching or exceeding one at the electron temperatures of typical operation. The sheath potential at the wall is likely on the order of $3T_e \approx 0.3V_d$ due to space charge and non-Maxwellian electron distribution function effects. However, the lower sheath potential at the wall increases the electron flux, which results in increased power loading at the wall.

The wall material selection, therefore, is a trade off between efficiency and life. Dielectric walls reduce the bombarding ion energy of the wall at the expense of higher electron fluxes and higher power loading. Metallic-wall Hall thrusters have higher ion energies to the wall and therefore sputter-erosion life issues, and so they have to compensate with geometry changes to obtain the desired life. This results in higher heat fluxes to the anode, which dominates the TAL efficiency. An increase in the power of both types of thrusters also requires increases in the thruster size to obtain the same or longer lifetimes. Therefore, Hall thruster design, like ion thruster design, is a trade off between performance and life.

References

[1] S. D. Grishin and L. V. Leskov, *Electrical Rocket Engines of Space Vehicles*, Moscow, Russia: Mashinostroyeniye Publishing House (published in Russian) , 1989.

[2] H. R. Kaufman, "Technology of Closed-Drift Thrusters," *AIAA Journal*, vol. 23, no. 1, pp. 78–87, 1985.

[3] V. V. Zhurin, H. R. Kaufman, and R. S. Robinson, "Physics of Closed Drift Thrusters," *Plasma Sources Science and Technology*, vol. 8, no. 1, pp. R1–R20, 1999.

[4] V. Kim, "Main Physical Features and Processes Determining the Performance of Stationary Plasma Thrusters," *Journal of Propulsion and Power*, vol. 14, no. 5, pp. 736–743, 1998.

[5] A. I. Morosov and V. V. Savelyev, "Fundamentals of Stationary Plasma Thruster Theory," in *Reviews of Plasma Physics*, edited by B. B. Kadomtsev and V. D. Shafranov, vol. 21, New York: Kluwer Academic/Plenum Publishers, 2000.

[6] J. R. Brophy, J. W. Barnett, J. M. Sankovic, and D. A. Barnhart, "Performance of the Stationary Plasma Thruster: SPT-100," AIAA-92-3155, 28th Joint Propulsion Conference, Nashville, Tennessee, July 6–8, 1992.

[7] B. A. Arhipov, L. Z. Krochak, S. S. Kudriavcev, V. M. Murashko, and T. Randolph, "Investigation of the Stationary Plasma Thruster (SPT-100) Characteristics and Thermal Maps at the Raised Discharge Power," AIAA-98-3791, 34th Joint Propulsion Conference, Cleveland, Ohio, July 13–15, 1998.

[8] L. B. King, "A Re-examination of Electron Motion in Hall Thruster Fields," IEPC-2005-258, 29th International Electric Propulsion Conference, Princeton University, New Jersey, October 31–November 4, 2005.

[9] R. R. Hofer, R. S. Jankovsky, and A. D. Gallimore, "High-Specific Impulse Hall Thrusters, Part 1: Influence of Current Density and Magnetic Field," *Journal of Propulsion and Power*, vol. 22, no. 4, pp. 721–731, 2006.

[10] R. R. Hofer and A. D. Gallimore, "High-Specific Impulse Hall Thrusters, Part 2: Efficiency Analysis," *Journal of Propulsion and Power*, vol. 22, no. 4, pp. 732–740, 2006.

[11] R. R. Hofer, "Development and Characterization of High-Efficiency, High-Specific Impulse Xenon Hall Thrusters," Ph.D. Dissertation, Aerospace Engineering, University of Michigan, Ann Arbor, Michigan, 2004.

[12] A. I. Morozov, Y. V. Esipchuk, A. M. Kapulkin, V. A. Nevrovskii, and V. A. Smirnov, "Effect of the Magnetic Field on a Closed-Electron-Drift Accelerator," *Soviet Physics Technical Physics*, vol. 17, no. 3, 1972.

[13] Y. Raitses, J. Ashkenazy, and M. Guelman, "Propellant Utilization in Hall Thrusters," *Journal of Propulsion and Power*, vol. 14, no. 2, pp. 247–253, 1998.

[14] L. A. Dorf, Y. F. Raitses, A. N. Smirnov, and N. J. Fisch, "Anode Fall Formation in a Hall Thruster," AIAA-2004-3779, 40th Joint Propulsion Conference, Ft. Lauderdale, Florida, July 11–14, 2004.

[15] L. Dorf, Y. Raitses, and N. J. Fisch, "Experimental Studies of Anode Sheath Phenomena in a Hall Thruster Discharge," *Journal of Applied Physics*, article 103309, part 1, vol. 97, no. 10, 2005.

[16] L. Dorf, Y. Raitses, and N. J. Fisch, "Effect of Magnetic Field Profile on the Anode Fall in a Hall-Effect Thruster Discharge," *Physics of Plasmas*, article 057104, vol. 13, no. 5, 2006.

[17] R. R. Hofer, P. Y. Peterson, A. D. Gallimore, and R. S. Jankovsky, "A High Specific Impulse Two-Stage Hall Thruster with Plasma Lens Focusing," IEPC-2001-036, 27th International Electric Propulsion Conference, Pasadena, California, October 14–19, 2001.

[18] J. A. Linnell and A. D. Galimore, "Krypton Performance Optimization in High-Voltage Hall Thrusters," *Journal of Propulsion and Power*, vol. 22, no. 4, pp. 921–925, 2006.

[19] J. A. Linnell and A. D. Galimore, "Efficiency Analysis of a Hall Thruster Operating with Krypton and Xenon Thrusters," *Journal of Propulsion and Power*, vol. 22, no. 6, pp. 1402–1412, 2006.

[20] Y. Daren, D. Yongjie, and Z. Shi, "Improvement on the Scaling Theory of the Stationary Plasma Thruster," *Journal of Propulsion and Power*, vol. 21, no. 1, pp. 139–143,2005.

[21] V. Kim, G. Popov, B. Arkhipov, V. Murashko, O. Gorshkov, A. Koroteyev, V. Garkusha, A. Semenkin, and S. Tverdokhlebov, "Electric Propulsion Activity in Russia," IEPC-2001-005, 27th International Electric Propulsion Conference, Pasadena, California, October 14–19, 2001.

[22] A. I. Bugrova, N. Maslennikov, and A. I. Morozov, "Similarity Laws for the Global Properties of a Hall Accelerator," *Journal of Technical Physics*, vol. 61, no. 6, pp. 45–51, 1991.

[23] V. Khayms and M. Martinez-Sanchez, "Design of a Miniaturized Hall Thruster for Microsatellites," AIAA-1996-3291, 32nd Joint Propulsion Conference, Lake Buena Vista, Florida, July 1–3, 1996.

[24] O. Gorshkov, "Russian Electric Propulsion Thruster Today," *Russian Space News*, vol. 61, no. 7, pp. 5–11, 1999.

[25] A. Smirnov, Y. Raitses, and N.J. Fisch, "Parametric Investigations of Miniaturized Cylindrical and Annular Hall Thrusters," *Journal of Applied Physics*, vol. 92, no. 10, pp. 5673–5679, 2002.

[26] M. Keidar, A. D. Gallimore, Y. Raitses, and I. D. Boyd, "On the Potential Distribution in Hall Thrusters," *Applied Physics Letters*, vol. 85, no.13, pp. 2481–2483, 2004.

[27] L. B. King and A. D. Gallimore, "Ion Energy Diagnostics in the Plasma Exhaust Plume of a Hall Thruster," *Journal of Propulsion and Power*, vol. 16, no. 5, pp. 916–922, 2000.

[28] J. E. Pollard, K. D. Diamant, V. Khayms, L. Werthman, D. Q. King, and K. H. Degrees, "Ion Flux, Energy and Charge State Measurements for the BPT-4000 Hall Thruster," AIAA-2001-3351, 37th Joint Propulsion Conference, Salt Lake City, Utah, July 8–11, 2001.

[29] C. E. Garner, J. R. Brophy, J. E. Polk, S. Semenkin, V. Garkusha, S. Tverdokhlebov, and C. Marrese, "Experimental Evaluation of Russian Anode Layer Thrusters," AIAA-1994-3010, 30th Joint Propulsion Conference, Indianapolis, Indiana, June 27–29, 1994.

[30] J. M. Fife, M. Martinez-Sanchez, and J. Szabo "A Numerical Study of Low-Frequency Discharge Oscillations in Hall Thrusters," AIAA-97-3052, 33rd Joint Propulsion Conference, Seattle, Washington, July 6–9, 1997.

[31] E. Y. Choueiri, "Fundamental Difference Between Two Variants of Hall Thrusters: SPT and TAL," *Physics of Plasmas*, vol. 8, no. 11, pp. 5025–5033, 2001.

[32] J. P. Bugeat and C. Koppel, "Development of a Second Generation of SPT," IEPC-95-035, 24th International Electric Propulsion Conference, Moscow, Russia, 1995.

[33] N. Gascon, M. Dudeck, and S. Barral, "Wall Material Effects in Stationary Plasma Thrusters: 1. Parametric Studies of an SPT-100," *Physics of Plasmas*, vol. 10, pp. 4123–4136, 2003.

[34] J. M. Fife and M. Martinez-Sanchez, "Comparison of Results from a Two-dimensional Numerical SPT Model with Experiment," AIAA-96-3197, 32nd Joint Propulsion Conference, Lake Buena Vista, Florida, July 1–3, 1996.

[35] J. M. Haas, "Low-Perturbation Interrogation of the Internal and Near-Field Plasma Structure of a Hall Thruster Using a High-speed Probe Positioning System," Ph.D. Dissertation, University of Michigan, Ann Arbor, Michigan, 2001.

[36] J. A. Linnell and A. D. Gallimore, "Internal Langmuir Probe Mapping of a Hall Thruster with Xenon and Krypton Propellant," AIAA-2006-4470, 42nd Joint Propulsion Conference, Sacramento, California, July 9–12, 2006.

[37] E. Ahedo, P. Martinez-Cerezo, and M. Martinez-Sanchez, "One-Dimensional Model of the Plasma Flow in a Hall Thruster," *Physics of Plasmas*, vol. 8, no. 6, pp. 3058–3068, 2001.

[38] E. Ahedo, "Presheath/Sheath Model with Secondary Electron Emission from Two Parallel Walls," *Physics of Plasmas*, vol. 9, pp. 4340–4347, 2002.

[39] G. D. Hobbs and J. A. Wesson, "Heat Flow Through a Langmuir Sheath in the Presence of Electron Emission," *Plasma Physics*, vol. 9, pp. 85–87, 1967.

[40] V. Baranov, Y. Nazarenko, and V. Petrosov, "The Wear of the Channel Walls in Hall Thrusters", IEPC-2001-005, 27th International Electric Propulsion Conference, Pasadena, California, October 14–19, 2001.

[41] E. Ahedo, J. M. Gallardo, and M. Martinez-Sanchez, "Effects of the Radial Plasma-Wall Interaction on the Hall Thruster Discharge," *Physics of Plasmas*, vol. 10, no. 8, pp. 3397–3409, 2003.

[42] J. M. Fife and S. Locke, "Influence of Channel Insulator Material on Hall Thruster Discharges: A Numerical Study," AIAA-2001-1137, 39th Aerospace Sciences Meeting, Reno, Nevada, January 8–11, 2001.

[43] Y. Raitses, D. Staack, M. Keidar, and N. J. Fisch, "Electron-Wall Interaction in Hall Thrusters," 057104, *Physics of Plasmas*, vol. 12, 2005.

[44] I. D. Kaganovich, Y. Raitses, D. Sydorenko, and A. Smolyakov, "Kinetic Effects in Hall Thruster Discharge," AIAA-2006-3323, 42th Joint Propulsion Conference, Sacramento, California, July 9–12, 2006.

[45] N. B. Meezan and M. A. Capelli, "Kinetic Study of Wall Collisions in a Coaxial Hall Discharge," *Physical Review E*, 036401, vol. 66, 2002.

[46] E. Ahedo and F. I. Parra, "Partial Trapping of Secondary Electron Emission in a Hall Thruster Plasma," *Physics of Plasmas*, 073503, vol. 12, no. 7, 2005.

[47] E. Ahedo and V. DePablo, "Effects of Electron Secondary Emission and Partial Thermalization on a Hall Thruster," AIAA-2006-4328, 42nd Joint Propulsion Conference, Sacramento, California, July 9–12, 2006.

[48] M. T. Domonkos, A. D. Gallimore, C. M. Marrese, and J. M. Haas, "Very-Near-Field Plume Investigation of the Anode Layer Thruster," *Journal of Propulsion and Power*, vol. 16, pp. 91–98, 2000.

[49] A. V. Semenkin, S. O. Tverdokhlebov, V. I. Garkusha, A. V. Kochergin, G. O. Chislov, B. V. Shumkin, A. V. Solodukhin, and L. E. Zakharenkov, "Operating Envelopes of Thrusters with Anode Layer," IEPC-2001-013, 27th International Electric Propulsion Conference, Pasadena, California, October 14–19, 2001.

[50] D. T. Jacobson, R. S. Jankovsky, and R. K. Rawlin, "High Voltage TAL Performance," AIAA-2001-3777, 37th Joint Propulsion Conference, Salt Lake City, Utah, July 8–11, 2001.

[51] A. E. Solodukhin, A. V. Semenkin, S. O. Tverdohlebov, and A. V. Kochergin, "Parameters of D-80 Anode Layer Thruster in One and Two-Stage Operation Modes," IEPC-2001-032, 27th International Electric Propulsion Conference, Pasadena, California, October 14–19, 2001.

[52] M. Hirakawa and Y. Arakawa, "Numerical Simulation of Plasma Particle Behavior in a Hall Thruster," AIAA-96-3195, 32nd Joint Propulsion Conference, Lake Buena Vista, California, July 1–3, 1996.

[53] J. P. Boeuf and L. Garrigues, "Low Frequency Oscillations in a Stationary Plasma Thruster," *Journal of Applied Physics*, vol. 84, pp. 3541–3554, 1998.

[54] E. Ahedo, "One-Dimensional Plasma Structure in Hall Thrusters," AIAA-98-8788, 34th Joint Propulsion Conference, Cleveland, Ohio, July 13–15, 1998.

[55] I. Mikellides, I. Katz, and M. Mandell, "A 1-D Model of the Hall-Effect Thruster with an Exhaust Region," AIAA-2001-3505, 37th Joint Propulsion Conference, Salt Lake City, Utah, July 8–11, 2001.

[56] S. Barral, K. Makowski, Z. Peradzynski, N. Gascon, and M. Dudeck, "Wall Material Effects in Stationary Plasma Thrusters. II. Near-Wall and In-Wall Conductivity," *Phys. Plasmas*, vol. 10, no. 10, pp. 4137–4152, 2003.

[57] F. I. Parra, E. Ahedo, J. M. Fife, and M. Martinez-Sanchez, "A Two-Dimensional Hybrid Model of the Hall Thruster Discharge," *Journal of Applied Physics*, 023304, vol. 100, 2006.

[58] M. Gamero-Castano and I. Katz, "Estimation of Hall Thruster Erosion Using HPHall," IEPC-2005-303, 29th International Electric Propulsion Conference, Princeton University, New Jersey, October 31–November 4, 2005.

[59] R. R. Hofer, I. Katz, I. G. Mikellides, and M. Gamero-Castano, "Heavy Particle Velocity and Electron Mobility Modeling in Hybrid-PIC Hall Thruster Simulations," AIAA-2006-4658, 42nd Joint Propulsion Conference, Sacramento, California, July 9–12, 2006.

[60] D. Manzella, J. Yim, and I. Boyd, "Predicting Hall Thruster Operational Lifetime," AIAA-2004-3953, 40th Joint Propulsion Conference, Ft. Lauderdale, Florida, July 11–14, 2004.

[61] C. Boniface, L. Garrigues, G. J. M. Hagelaar, and J. P. Boeuf, "Anomalous Cross Field Electron Transport in a Hall Effect Thruster," *Applied Physics Letters*, 161503, vol. 89, 2006.

[62] E. Y. Choueiri, "Plasma Oscillations in Hall Thrusters," *Phys. of Plasmas*, vol. 8, no. 4, pp. 1411–1426, 2001.

[63] A. Ducrocq, J. C. Adam, A. Heron, and G. Laval, "High-Frequency Electron Drift Instability in the Cross-field Configuration of Hall Thrusters," *Physics of Plasmas*, 102111, vol. 13, 2006.

[64] V. Abgaryan, H. Kaufman, V. Kim, D. Ovsyanko, I. Shkarban, A. Semenov, A. Sorokin, and V. Zhurin, "Calculation Analysis of the Erosion of the Discharge Chamber Walls and Their Contamination During Prolonged SPT Operation," AIAA-94-2859, 30th Joint Propulsion Conference, Indianapolis, Indiana, June 27–29, 1994.

[65] Y. Garnier, V. Viel, J. F. Roussel, and J. Bernard, "Low Energy Xenon Ion Sputtering of Ceramics Investigated for Stationary plasma Thrusters," *Journal of Vacuum Science Technology A*, vol. 17, pp. 3246–3254, 1999.

[66] Y. Yamamura and H. Tawara, "Energy Dependence of Ion-Induced Sputtering from Monatomic Solids at Normal Incidence," *Atomic Data and Nuclear Data Tables*, vol. 62, pp. 149–253, 1996.

[67] S. K. Absalamov, V. Andrew, T. Colberi, M. Day, V. V. Egorov, R. U. Gnizdor, H. Kaufman, V. Kim, A. I. Korakin, K. N. Kozubsky, S. S. Kudravzev, U. V. Lebedev, G. A. Popov, and V. V. Zhurin, "Measurement of Plasma Parameters in the Stationary Plasma Thruster (SPT-100) Plume and its Effect on Spacecraft Components," AIAA-1992-3156, 28th Joint Propulsion Conference, Nashville, Tennessee, July 6–8, 1992.

Homework Problems

1. You want to design an experimental Hall thruster to operate from 100 to 800 V and from 100 to 300 gauss. Assuming that the electron temperature is always about 10% of the discharge voltage, what are the minimum and maximum lengths of the magnetized region in the channel to have a factor of 5 margin against electron and ion orbit limits? Neglect collisions.

2. Derive Eq. (7.3-42).

3. A Hall thruster has a plasma channel with a 15-cm outer diameter and a 10-cm inner diameter. Measurements made on the thruster indicate that the xenon plasma density in the channel is 5×10^{17} ions per m^3, the electron temperature T_e is 20 eV, and the radial magnetic field B_r is 200 gauss (0.02 tesla). If the thruster is operated at a discharge voltage of 300 V,
   a. What is the beam power?
   b. What is the electron Larmour radius r_L ?
   c. What is the electron Hall parameter Ω_e ?
   d. If the thrust correction factor $\gamma = 0.9$ and the mass utilization efficiency $\eta_m = 0.8$, what is the thrust and Isp?
   e. What is the Hall current?
4. A xenon Hall thruster has boron nitride walls with a linearly varying secondary electron yield with a value of 0.5 at zero electron energy and 2 for an electron energy of 100 eV.
   a. What is the equation for the secondary electron yield in terms of the electron energy?
   b. Find the equation for the secondary electron yield for a Maxwellian distribution of electron energies [hint: use Eq. (C-5)] in terms of the electron temperature T_e.
   c. What is the electron temperature at which the electron flow to the wall is space-charge limited?
   d. Assuming $n_e v_B / n_i v_i = 0.5$, what is the maximum sheath potential for non-space-charge-limited flow (T_e less than the value found in part b)?
5. Assume that all the ions in a Hall thruster are produced by the Hall current ionizing the neutral gas in the channel.
   a. Neglecting the ion current to the wall as small so that all the ions produced become beam ions, what is the ratio of the Hall current to the beam current if the average electron temperature is 25 eV? (Hint: write the ion production rate in terms of the Hall current and use Appendix E for ionization and excitation collision cross sections.)
   b. For a xenon ion thruster with a mean radius of 9 cm, a radial magnetic field of 150 G, and a discharge voltage of 300 V, what is the ratio of the Hall current to the beam current?

6. A xenon Hall thruster has a channel outside diameter of 10 cm and a channel width of 3.5 cm with $BNSiO_2$ walls. Assume a plasma density of 2×10^{17} m^{-3} and an electron temperature of 20 eV in the channel with the majority of the plasma in contact with 1 cm of the wall axially.
   a. What is the electron current to the wall?
   b. What is the net electron current to the wall?
   c. What is the power deposited on the wall associated with this electron current?
   d. What is the power deposited on the wall associated with ion current?
7. Assume that the thruster in Problem 6 has alumina walls and produces 3.5 A of beam current at 400 V with an electron temperature in the channel of 15 eV. The thruster also has a beam current utilization efficiency $\eta_b = 0.5$.
   a. What is the power into the discharge?
   b. What is the total power into the alumina walls for a contact length L = 2 cm?
   c. Assuming that the electron temperature at the anode is 5 eV, the mass utilization efficiency is 90%, and the thrust correction factor $\gamma = 0.9$, and neglecting all other power loss channels, what is the thruster efficiency?
   d. For a beam voltage utilization efficiency of 0.9, how much thrust and Isp is produced?
8. The electron current to the anode in a Hall thruster can be estimated from the perpendicular electron flux diffusing through the plasma channel.
   a. Neglecting the pressure gradient terms, derive an expression for the current toward the anode in terms of the collision frequency in the channel plasma.
   b. For the thruster in Problem 7 with a transverse magnetic field of 150 G and an axial electric field of 3×10^4 V/m, what is the anode current if only classic electron–ion collisions are considered?
   c. The effective wall collision frequency can be estimated as the electron current to the wall times the secondary electron yield and divided by the total number of particles in the plasma ($v_w = \gamma I_{ew} / N$, where N is approximately the plasma density times the channel cross-sectional area times the plasma length L). Derive an expression for the transverse electron current due to the electron-wall collisions in terms of the electron current to the wall.

d. What is the total transverse electron current for this thruster example, using $L = 1$ cm for the bulk of the plasma density?

e. If the walls are made of $BNSiO_2$, what is the anode current? Why does it depend so strongly on the wall material?

9. Calculate the power lost to the wall in a xenon TAL thruster with stainless steel walls that has a plasma density at the sheath edge of 2×10^{17} m^{-3} and an electron temperature of 20 eV. The channel has a 12-cm outside diameter, an 8-cm inside diameter, and is 0.5-cm long. Which power loss channel (ions or electrons) is larger?

10. The life of a TAL thruster is limited primarily by the ion sputtering of the metallic guard rings next to the thruster exit. Assume a TAL has a plasma density near the wall of 10^{17} m^{-3} and an electron temperature of 25 eV.

a. For stainless steel walls, what is the ion current density to the walls (the guard rings) and the sheath potential?

b. Assuming that the stainless-steel sputtering yield is about 0.1 atoms per incident ion at the sheath voltage found in (a), what is the life in hours of the TAL if 2-mm thickness of the stainless-steel guard ring material can be eroded away?

c. Assume that the wall material has been changed to graphite with a secondary electron yield of about 0.5. What is the sheath potential at the wall?

d. Assuming that the graphite sputtering yield is about 5×10^{-3} atoms per incident ion at the sheath voltage found in (c), what is the life in hours of the TAL if 1-mm thickness of the graphite guard ring material can be eroded away?